The molecular scale structure of electrode-electrolyte interfaces: the case of platinum in aqueous sulfuric acid

Cheng Hao Wu[1,2]‡, Tod A. Pascal[3]‡, Artem Baskin[3], Huixin Wang[2,4], Hai-Tao Fang[2,4], Yi-Sheng Liu[5], Yi-Hsien Lu[2], Jinghua Guo[5,6], David Prendergast[3], and Miquel B. Salmeron[2,7,*]

[1] Department of Chemistry, University of California, Berkeley, Berkeley CA, USA
[2] Materials Science Division, Lawrence Berkeley National Laboratory, Berkeley CA, USA
[3] The Molecular Foundry, Lawrence Berkeley National Laboratory, Berkeley CA, USA
[4] School of Materials Science and Engineering, Harbin Institute of Technology, Harbin, P. R. China
[5] The Advanced Light Source, Lawrence Berkeley National Laboratory, Berkeley CA, USA
[6] Department of Chemistry and Chemical Biology, University of California, Santa Cruz, Santa Cruz CA, USA
[7] Department of Materials Science and Engineering, University of California, Berkeley, Berkeley CA, USA

‡These authors contributed equally to this work

*Corresponding Email: mbsalmeron@lbl.gov

Abstract

Knowledge of the molecular composition and electronic structure of electrified solid-liquid interfaces is key to understanding elemental processes in heterogeneous reactions. Using x-ray absorption spectroscopy in the interface-sensitive electron yield mode (EY-XAS), first-principles electronic structure calculations, and multiscale simulations, we determined the chemical composition of the interfacial region of a polycrystalline platinum electrode in contact with aqueous sulfuric acid solution at potentials between the hydrogen and oxygen evolution reactions. We found that between 0.7 and 1.3V vs Ag/AgCl the electric double layer (EDL) region comprises adsorbed sulfate ions (SO_4^{2-}) with hydrated hydronium ions (H_3O^+) in the next layer. No evidence was found for bisulfate (HSO_4^-) or Pt-O/Pt-OH species, which have very distinctive spectral signatures. In addition to resolving the long-standing issue of the EDL structure, our work establishes interface- and element-sensitive EY-XAS as a powerful spectroscopic tool for studying condensed phase, buried solid-liquid interfaces relevant to various electrochemical processes and devices.

1. Introduction

Knowledge of the molecular structure and composition of solid-liquid interfaces is of fundamental importance for an atomic-level understanding of the interfacial processes of corrosion, geochemistry, atmospheric chemistry, (photo)electro-catalysis and energy storage systems.[1–3] Renewed interest in interfaces and interfacial phenomena, due in part to the impetus for efficient storage of the energy produced by intermittent renewable sources has spurred numerous studies using a variety of techniques, including electrochemical analysis,[2,4–6] radio-tracer methods,[7–9] electrochemical quartz crystal micro-balance (EQCM),[10–12] and interface-sensitive microscopies and spectroscopies including scanning probe microscopy,[13] surface-sensitive vibrational spectroscopies,[14–16] surface x-ray scattering[17,18] and surface extended x-ray absorption fine structure (SEXAFS),[1] to name a few. However, interpretation of the data obtained with these techniques often relies on assumptions about the speciation and molecular structure of superficial layers based on thermodynamic arguments or models that are not been substantiated at the atomic level. As a result, understanding the dynamic molecular structure of buried functional electrochemical interfaces remains a great challenge.

Of particular interest is the prototypical interface between platinum and aqueous sulfuric acid [Pt-H_2SO_4(aq)]. Despite the substantial amount of data on Pt electrodes in numerous forms,[2,19,20] the interfacial composition and speciation at the Pt-H_2SO_4(aq) interface under various potentials remain unresolved. There is general consensus on the composition of the polycrystalline Pt-H_2SO_4(aq) interface at potentials E < 0.8V vs RHE (or E_{RHE}).[7,15,16,21,22] In the anodic potential range (E_{RHE} > 0.8V) however, the surface structure of the Pt electrode and the composition of the electric double layer (EDL) are still debated. In the conventional model, the evolution of the Pt-H_2SO_4(aq) interface is described as follows: (1) Initial adsorbates at the Pt-H_2SO_4(aq) interface at E_{RHE} > 0.8V are assumed to be bisulfate (HSO_4^-) anions,[23] based on the fact that HSO_4^- dominates the speciation in dilute

H_2SO_4 solutions, or a mixture of SO_4^{2-} and HSO_4^- coadsorbed with water and/or hydronium, a poorly defined system referred to as (bi)sulfate. (2) The (bi)sulfate species desorb with increasing anodic potentials, displaced by atomic oxygen (-O) and/or hydroxyl groups (-OH).[4–6,10,23–25] (3) Accumulation of -O/-OH at more positive potentials further excludes (bi)sulfate ions from Pt surface and leads to the formation of three-dimensional layers of $PtO_x/Pt(OH)_x$.[4–6,26]

Studies using previously mentioned characterization techniques have provided evidence supporting many aspects of the conventional model, but the picture of the Pt-H_2SO_4(aq) interface remains incomplete with several important questions unanswered, in particular, the chemical nature of the surface oxide/hydroxide. EQCM measurements[10–12] have confirmed mass addition onto the Pt surface at E_{RHE} > 0.8V; however the assignment of the added mass typically relies on presumed speciation at the interface. X-ray scattering and SEXAFS experiments [18,27,28] successfully detected variations in electron density with increasing E_{RHE} to above 0.8V, which were typically interpreted as resulting from surface oxide formation. Nevertheless, the electron density in this case is dominated by heavy elements, such as Pt, which makes these measurements less deterministic for light elements such as O or S.[35] S-labeled radiotracer experiments[7–9] indicated that (bi)sulfate ions adsorb on the Pt surface around E_{RHE} ~0.8V and partially desorb at higher potentials, presumably replaced by surface oxide/hydroxide. Such a conclusion, especially on the sulfate adsorption, is also in line with a number of vibrational spectroscopy studies.[15,16,29,30] However, some in-situ IR studies,[15,23,31,32] together with several single crystal EC-STM, [19,21] have called into question the formation of such a surface oxide. In addition, a recent surface-enhanced infrared absorption spectroscopy study[15] found that at anodic potentials the ν(OH) band of interfacial water molecules remains at ~3000cm^{-1}, instead of shifting to 3200cm^{-1} as expected for water molecules forming hydrogen-bonds with an oxide surface.

Recent technological advances have made possible to extend powerful microscopy and spectroscopy characterization techniques, such as transmission electron microscopy, x-ray photoelectron spectroscopy (XPS), and x-ray absorption spectroscopy (XAS), from vacuum to ambient environments and under applied bias, thus providing new opportunities for *operando* investigation of solid-liquid interfaces.[3,33–36] Here we use interface-sensitive electron-yield XAS (EY-XAS), based on measuring the drain current between solution and electrode resulting from the relaxation of core holes produced by absorption of X-rays.[3,33] The complexity of the absorption spectra however requires complementary first-principles electronic structure calculations for unambiguous interpretation. Here we apply this approach and extend it by including multiscale simulations to elucidate the long-standing question of the interfacial composition and speciation at the Pt-H_2SO_4(aq) interface. Our measurements and calculations indicate that under anodic potentials preceding oxygen evolution the interface region (1-2nm) is dominated by adsorbed sulfate ions (SO_4^{2-}), hydronium ions, and solvating water. In contrast to the conventional "oxide formation" model, we found no trace of Pt-O/Pt-OH or bisulfate (HSO_4^-) species within the sensitivity limit of the measurements. Our results call for a review of models of electrochemical interfaces based on conventional experimental methods that do not involve unambiguous, interface-sensitive spectroscopy.

2. Experimental Section

Thin films (~15nm) of Pt (or Au) working electrodes were deposited via e-beam evaporation onto x-ray transparent Si_3N_4 membrane windows (100nm in thickness). Prior to film deposition a 2nm Ti layer was deposited, also by e-beam evaporation, to act as an adhesion layer between the Si_3N_4 surface and the metal film. The films were polycrystalline with 2nm average corrugation, as shown by the AFM topographic images (Figure S1). The metal-covered Si_3N_4 window was then assembled in a liquid cell,[33] containing a Pt wire acting as a counter electrode and a miniature Ag/AgCl reference electrode (~0.25V vs RHE

in 0.05M H_2SO_4). *Operando* XAS measurements were performed at BL8.0.1.3 of the Advanced Light Source synchrotron facility at the Lawrence Berkeley National Laboratory. Bulk-sensitive total fluorescence yield (TFY) and interface-sensitive total electron yield (TEY) XAS spectra were collected simultaneously during each experiment.

Concurrent first-principles molecular dynamics (FPMD) calculations were performed, with the Pt electrode modeled by a 4×4×6 supercell of 96 atoms, with the (111) surface exposed to an aqueous solution comprising 119 water molecules and various amounts of sulfuric acid species (H_2SO_4, HSO_4^- and SO_4^{2-}), neutralized by appropriate amounts of H_3O^+ molecules. Umbrella sampling[37,38] free energy calculations were performed to determine the binding free energy of the individual sulfuric acid species to the Pt electrode. A description of the EDL at various surface charge densities with open boundary conditions was obtained from a self-consistent continuum model, based on a free energy functional and a modified Poisson-Boltzmann equation formalism.[39] Input parameters for the continuum model were provided by FPMD calculations. The simulated *K*-edge XAS of the various oxygen containing species were obtained using the eXcited electron and Core-Hole method,[40] critically employing a self-consistent energy alignment scheme[41] that allows us to unambiguously resolve the absolute XAS peak positions of different oxygen containing species in the unit cell.

More details regarding the experimental setup and computational procedure are described in the supplementary information.

3. Results and Discussion

3.1. XAS at the Pt-H_2SO_4(aq) interface

Using the liquid cell shown schematically in Fig. S1 for *operando* EY-XAS measurements, we collected cyclic voltammograms (CV) of our Pt electrode in 0.05M H_2SO_4 (Fig. S2). The CV is very similar to those published for polycrystalline platinum electrodes.[2] Notably,

between hydrogen desorption and oxygen evolution potentials a broad anodic wave starting around E = 0.6V vs Ag/AgCl (corresponding to E_{RHE} ~ 0.85V) is observed, followed by a strong peak around $E_{Ag/AgCl}$ = 0.5V in the cathodic sweep. These features have been commonly attributed to Pt oxide formation or -O/-OH adsorption, and oxide reduction, respectively.[2,4,10,42]

Under open circuit potential (OCP; typically 0.3-0.4V vs Ag/AgCl for a fresh Pt film), the O K-edge EY-XAS spectrum is similar to that found at the interface of the Au-H_2O system,[33] showing a substantial suppression of the pre-edge feature at 535eV (due to preferential water orientation and x-ray excited-state orbital hybridization with the metal substrate) compared to the bulk XAS spectra of pure water and H_2SO_4 solution (TFY spectra in Fig. S3). Such similarity indicates that at OCP the Pt-H_2SO_4(aq) interface is also dominated by water. This conclusion is supported by our equilibrium first-principles molecular dynamics (FPMD) simulations which reveal that the water density profile across the Pt-H_2SO_4(aq) interface in a 0.4M H_2SO_4 solution is similar to that of Pt-H_2O and Au-H_2O interfaces, with the first layer mass density peak at ~3Å (Fig. S4). At the Au-H_2O interface we also observed that negative bias potentials modify the hydrogen bonding network by increasing the fraction of water molecules with broken hydrogen bonds, resulting in a pronounced pre-edge feature.[35] We find a similar effect at both Pt-H_2SO_4(aq) and Au-H_2SO_4(aq) interfaces at voltages below the OCP (Figs. S5 and S6).

In the potential region more positive than the OCP ($E_{Ag/AgCl}$ > 0.3V), the O K-edge EY-XAS spectra of the Pt-H_2SO_4(aq) interface species (Fig. 1a) exhibit a pre-edge peak at 535eV. The position of this peak coincides with the pre-edge peak of water with broken hydrogen bonds, visible both in the spectra of bulk water and under negative potentials at the Au-H_2O interface, but notably absent under positive potentials. However, the pre-edge peak at Pt-H_2SO_4(aq) interface is narrower than the pre-edge feature at the Au-H_2O interface (Figs. S6 and S7), which appears as a shoulder in XAS spectra obtained using the

same apparatus with identical settings. Moreover, Fig. 1a shows that the pre-edge peak observed at the Pt-H_2SO_4(aq) interface at positive potentials becomes more intense with respect to the main edge peak (537eV) at higher potentials. These changes are reversible, as shown by the potential-dependence of pre-edge-to-main-edge ratio (I_{535eV}/I_{537eV}) (Fig.

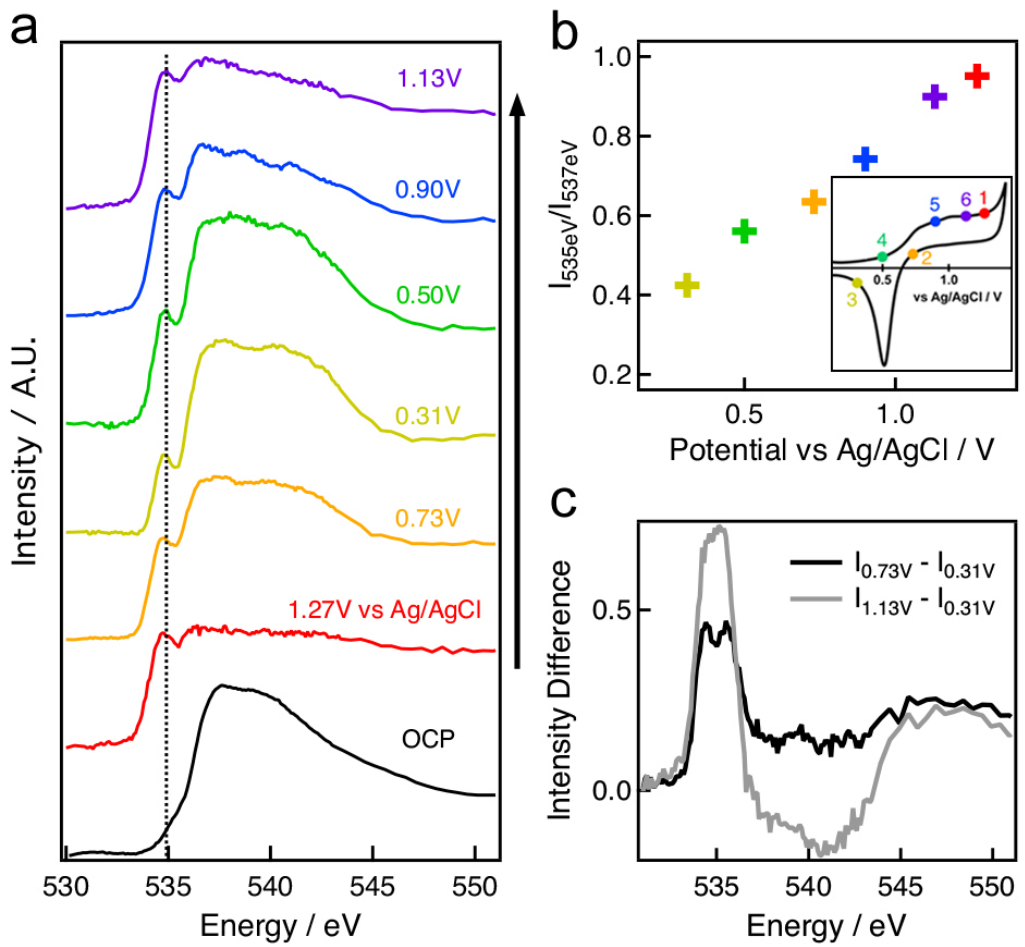

Figure 1. *Operando* XAS measurements at the Pt-H_2SO_4(aq) interface at open circuit and anodic potentials. (a) O K-edge EY-XAS spectra at different potentials. **(b)** Variation of the intensity ratio between the pre-peak (535 eV) and the main peak (537 eV) as a function of potential. The color of each data point matches the color of the spectrum from which the value was calculated. The inset shows the anodic part of Pt-H_2SO_4(aq) CV curve. The colored number indicates the order of the spectra acquisition. **(c)** Difference between the spectra measured at 0.73 V and 0.31 V, 1.13 V and 0.31 V (vs Ag/AgCl), respectively.

1b and S8): From 1.27V to 0.31V and back to 1.13V, the ratios follow roughly the same trend. Another variation in the spectra is the extension of the XAS post-edge plateau (>540eV) towards higher energy at more positive potentials, as exemplified by the intensity difference between spectra collected at 0.73V and 1.13V, and that at 0.31V (Fig. 1c), where a broad feature can be discerned above 540eV. At the highest potentials examined, 1.13V and 1.27V, the spectra exhibit a more extended flat tail that resembles saturation effects commonly observed in fluorescence or low-energy partial electron yield XAS.[43] This could be the result of substantial amount of low energy secondary electrons generated deeper in the solution reaching the electrode at higher positive potentials. As discussed in the supplementary materials (SM) however, this effect is not severe enough here to distort the EY-XAS spectra, at least for positive bias below ~1V.

3.2. Speciation and ion distribution at the Pt-H_2SO_4(aq) interface

To provide a molecular-scale model of the Pt-H_2SO_4(aq) interface we performed FPMD simulations paired with continuum thermodynamic models. From this we determined which of the multiple species, H_2O, H_3O^+, SO_4^{2-}, HSO_4^- and H_2SO_4,[44] are most likely to be present at the interface and contribute to the overall O K-edge spectra, and thus facilitate the interpretation of XAS spectra. The simulations revealed that in contact with low concentration of H_2SO_4 (~0.4M in the simulation, Fig. 2a), the dominant species on the neutral Pt surface are water molecules. A small number of sulfate anions reside close to the surface (~2.7Å) together with a small amount of H_3O^+ in the neighboring water layer (8-10Å). We note that even at this relatively low concentration in the simulation cell, the sulfate anions preferentially adsorb near the interface. For more concentrated H_2SO_4 solutions (~3.0M in the simulation), we find that sulfate ions displace interfacial water molecules, such that the surface density of sulfate anions surpasses that of water, with a concomitant increase in H_3O^+ concentration in the first interfacial layer (1.5 - 4.3Å), as shown in Fig. 2b. This is in line with free energy calculations in the thermodynamic

(infinite time) limit shown in Fig. S9a, which show a minimum at ~2.7Å from the Pt surface in the free energy profile of solvated SO_4^{2-} ions (similarly for HSO_4^- and H_2SO_4). Notably, the calculated binding free energy of an isolated SO_4^{2-} ion to the interface is a relatively weak -34.8kJ/mol/molecule at 298K. This is comparable to experimental estimates based on isotherms at equilibrium (~80%) surface coverage[26] of ~350kJ/mol, or equivalently 35 – 45 kJ/mol. Further, for the charge-neutral surface, our FPMD simulations further show

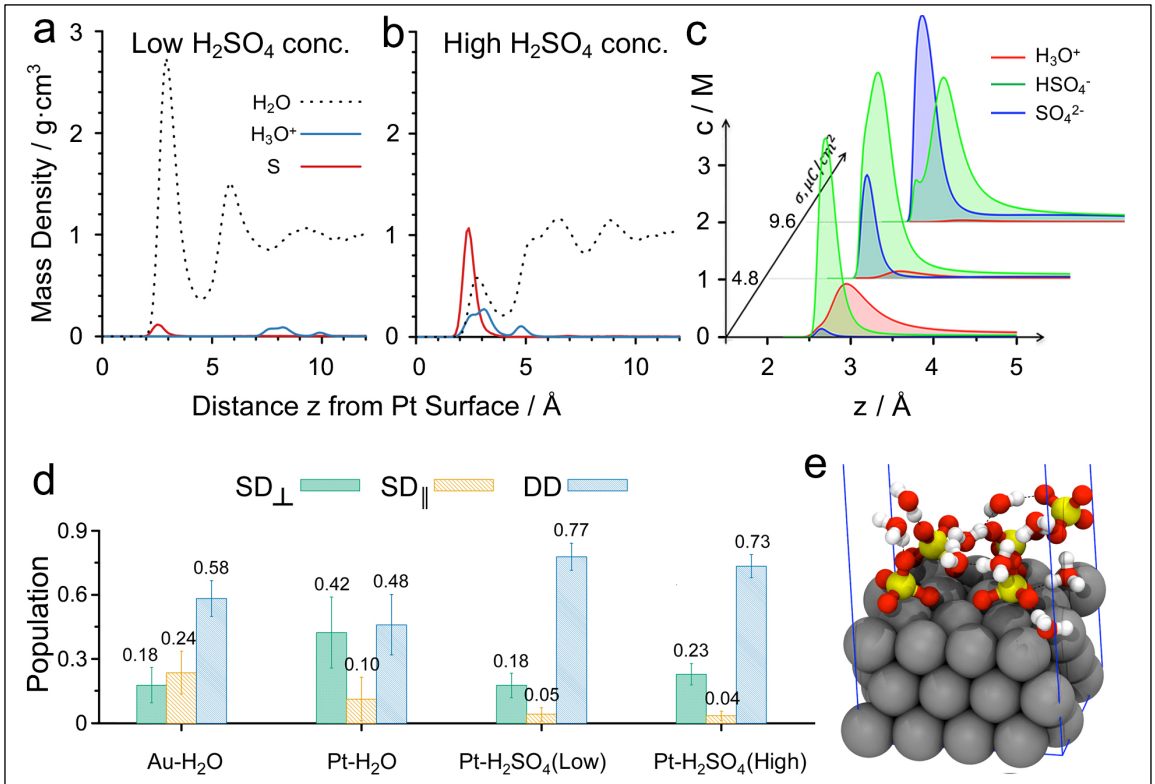

Figure 2. Structure of the Pt-H_2SO_4(aq) interface from first principles molecular dynamics (FPMD) and thermodynamic multiscale simulations. (a,b) Surface mass density profile of H_2O, H_3O^+, S in (**a**) low concentration (0.4M in the simulation cell) and (**b**) high concentration (3.0M in the simulation cell) sulfuric acid solutions. **(c)** Ion concentration profiles near a Pt electrode at various surface charge densities, from the continuum model with bulk H_2SO_4 concentration of 0.05 M. **(d)** Populations of water species of single and double donors, with configurations perpendicular and parallel to the surface (SD⊥, SD∥, DD) at interfaces between Au-H_2O, Pt-H_2O, and Pt-H_2SO_4 in 0.4M and 3.0M H_2SO_4 solution. **(e)** Representative snapshot of sulfuric acid at the Pt interface at high surface coverage (~84%). Water molecules beyond 0.5nm of the interface are removed for clarity.

that the adsorbed sulfate ions act as free rotors near the Pt interface, consistent with the experimental observation that at the potential of zero charge (PZC) (0.16 V vs. RHE) the S-O stretching frequencies of the adsorbed sulfate ions coincide with those of free ions.[23] At higher positive surface charge (i.e., more anodic potential), we expect increased population and more specific binding of the sulfate anions, as observed experimentally.[21,45]

We note that FPMD simulations have certain limitations in predicting molecular speciation at interfaces and realistically modelling biased interfaces, which arise from the periodic boundary and neutrality conditions used in the simulations, as well as the finite number of species in the simulation cells, and limited computation time. We overcome these limitations by developing a self-consistent continuum model (details in SM and Figs. S10-S11), which provide information about the distributions of ions for open systems under applied bias (Fig. 2c and S12). As shown in Fig. 2c and consistent with our FPMD simulations, this model predicts that although in the calculation the bulk concentration of H_2SO_4 was set to 0.05M, the interface concentration of sulfate and bisulfate species is substantially higher, even on the charge neutral surface. With increasing charge density on the electrode (or equivalently external bias), the surface density of HSO_4^- increases initially followed by a slow decay, as more SO_4^{2-} ions are attracted to the interface, eventually becoming the dominating surface species (Figs. 2c, S12, S13). These anions expel water molecules in the EDL and create a local environment with a higher pH than in the bulk solution.

Finally, we note that our FPMD calculations also indicate that the adsorption and accumulation of sulfate ions at the interface alters the hydrogen-bonding network of interfacial water molecules. We performed hydrogen bond statistical analysis, with the hydrogen bond defined by the method prescribed by Luzar and Chandler.[46] For each water molecule, we separately considered those with both hydrogens participating in hydrogen bonding with neighboring water molecules (double donors of DD), those with one broken

hydrogen bond (single donors) that are aligned either perpendicular ($SD^{\perp}$) or parallel ($SD^{\parallel}$) to the Pt surface, as well as those with two broken hydrogen bonds (no donors ND). As shown in Fig. 2d, sulfate adsorption at the Pt surface promotes hydrogen-bonding, leaving more fully-coordinated water molecules (double donor or DD species; 73-77% depending on concentration) compared to the case without sulfate ions (48%), as shown in Fig. 2d.

3.3. First principles simulated XAS of the Pt-H_2SO_4(aq) interface. Having determined the thermodynamic average speciation and molecular configurations at the interface allowed us to determine what molecular structural motifs give rise to the spectral signatures observed in experiment. To our knowledge no experimental O K-edge spectra have been obtained for solvated sulfate or hydronium species in the bulk solution, due to overwhelming signal from bulk water molecules. XAS spectra of sulfate salt crystals (Fig. S14) are not meaningful in this context because the electronic structure of the sulfate ions confined in a crystal matrix is different from that of mobile sulfate ions hydrogen-bonded to surrounding water molecules. Similarly, the XAS of highly concentrated H_2SO_4 is of little use due to the drastically different dissociation mechanism and coordination chemistry when very few water molecules are present. Moreover, electronic interactions between adsorbate and substrate can modify the XAS, as illustrated in the case of the Au-H_2O interface.[33] Therefore, first-principles XAS calculations[40] based on a self-consistent energy alignment scheme[41] were performed to provide atomic-scale insights into the molecular structure and electronic transitions that give rise to the observed spectra.

Fig. 3a presents the simulated XAS of the various species, including solvated H_3O^+, H_2SO_4, HSO_4^-, and SO_4^{2-}, as well as H_2O molecules with different configurations (double donor DD, single donor SD, and non-donor ND), both in the bulk solution and at the Pt-H_2SO_4(aq) interface. We find that H_2O molecules at the Pt interface have XAS signatures similar to those at the Au interface, where the intensity of the pre-edge feature at 535eV related to

SD species is suppressed due to delocalization of the molecular orbitals of excited H_2O molecules into the metal substrate.[33] On the other hand, the XAS features of solvated H_3O^+ ions, which are located in the second solvation layer and are thus not electronically coupled

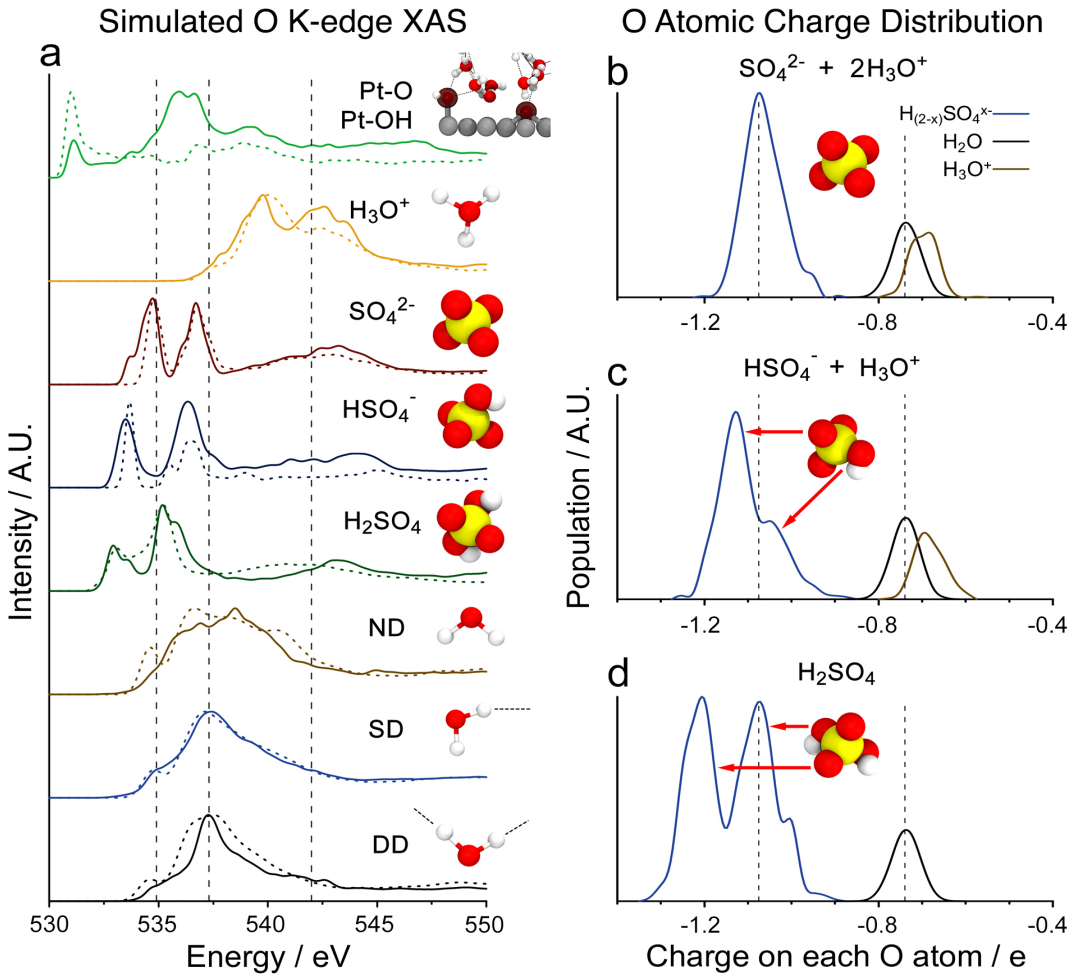

Figure 3. **Electronic structure and XAS simulations. (a)** O K-edge XAS spectra of various O-containing species at the Pt-H_2SO_4(aq) interface calculated from first principles. The XAS of each species at the interface (solid line) is compared to that in the bulk (dashed lines). Dashed vertical lines represent the energy of the three main XAS features of bulk water: the pre-edge near 535eV, the main edge near 537eV, and the post-edge near 541eV. **(b-d)** Charge distribution on the oxygen atoms in the various solvated sulfate species (blue), bulk water (black), and H_3O^+ (brown) from Bader charge analysis of bulk systems. Dashed vertical lines indicate the average partial charges on each oxygen atom in the SO_4^{2-} ions (-1.07e$^-$) and in water molecules (-0.74e$^-$).

to the metal band structure are blue shifted to the region above 537 eV compared to those of water, reflecting the core-level chemical shift due to the additional H^+ (Fig. 3b and c).

The simulated XAS of the SO_4^{2-} anion is characterized by two prominent peaks at 534.5 and 537eV, which align closely to the pre-edge and main-edge peaks of bulk water. These XAS spectral signatures do not shift appreciably with different amounts of positive surface charge on the Pt-electrode (Fig. S15). A similar pair of prominent peaks are present in the simulated spectrum of the solvated HSO_4^- ion but red-shifted to ~533 and ~536eV and would be clearly distinguishable from SO_4^{2-} spectrum. Analysis of the ground state electron density (Fig. 3c) of the solvated HSO_4^- ions reveals an asymmetric charge distribution among the four oxygen atoms: the three non-protonated oxygen atoms have increased electron charge density (-0.05e on average), whereas the oxygens in the -OH group have slightly less electron density (+0.01e on average) compared to SO_4^{2-}. This splits the degeneracy and results in an additional pair of blue-shifted features at ~534 and ~537eV associated with excitations involving oxygen atoms in the -OH group. However, the -OH group actively participates in hydrogen bonding with the surrounding water molecules, and the resulting core-excited state is delocalized over several molecules. Such delocalization substantially reduces its XAS intensity and makes the feature at 534eV completely overwhelmed by a main peak of non-protonated oxygen atoms at 533eV. The simulated XAS of H_2SO_4 species next to the Pt interface show quantum mechanical effects even more pronounced than in HSO_4^-, manifested in the red-shift to 532.5 and 535.5eV of the peaks associated with non-protonated oxygen atoms. Similarly, because of the increased electron density on these atoms in the ground state the excitations involving the protonated oxygen atoms display two prominent shoulders at energies slightly higher than the main peaks.

The simulated XAS of solvated Pt-O/Pt-OH species, at the top of Fig. 3a, exhibit a distinctive spectroscopic signature: a sharp peak at ~531eV, resulting from O1*s* → hybridized O2*p*-Pt5*d* transitions. These spectral features are prominent because the core-

excited states are localized along the Pt-O(H) bonds, which are primarily ionic with occupied orbitals that lie deep in the valence band. These calculated Pt-O(H) XAS spectra are consistent with experimental partial electron yield XAS results from various surface Pt oxides measured with ambient-pressure XPS under partial pressure of O_2 gas.[47]

3.4. The structure of the Pt-H_2SO_4(aq) interface at anodic potentials

Our multiscale theoretical analysis of the thermodynamics and corresponding XAS simulations provide strong evidence for the preferential adsorption of sulfate species at the Pt-H_2SO_4(aq) interface, especially at positive potentials. The increase in the surface density of both SO_4^{2-} and H_3O^+ ions obtained in the simulations is in line with the observed growth of the sharp peak around 535eV and the features at and above 540eV, as illustrated in the composite simulated XAS spectra using the speciation from our equilibrium FPMD simulations at various sulfate concentrations (0, low, and high; Fig. 4b) with the experimental XAS spectra at different potentials (OCP, 0.31V, and 1.13V vs Ag/AgCl; Fig. 4a). The pre-edge feature observed at anodic potentials originates from the SO_4^{2-} ions alone, with no contribution from interfacial H_2O molecules. This is because the H_2O reorientation behavior at the positively charged surface results in a suppressed pre-peak, as demonstrated in the case of Au-H_2O.[33]

Of particular interest is the lack of evidence for the existence of Pt-O(H) layers in our experimental spectra, even at the highest potential tested here ($E_{Ag/AgCl}$ = 1.27V). This finding goes against the widely-accepted model of competitive replacement of adsorbed anions by oxygenated species and formation of oxide/hydroxide at the Pt-H_2SO_4(aq) interface at E_{RHE} > 0.8V. It is also hard to justify the desorption of sulfate anions from the more positively charged surface due to competitive -O(H) adsorption.[8,26] Given the relatively weak Pt-OH_{ads} bonding compared to the strength of the Pt-O bond, estimated to be 136 - 225 kJ/mol and ~ 350 kJ/mol respectively[26] at equilibrium coverage, one would

conclude that sulfate and bisulfate anions that provide two or three bonding oxygen atoms should be the dominant species at increasingly positive potentials. Indeed, *in situ* vibrational spectroscopy studies[16,23,31] confirmed the adsorption of sulfate ions on the Pt surface and its increase with potential, with no sulfate desorption. EC-STM studies on flat single crystals (e.g., Pt, Au, Pd, and Cu)[19,21,45] also provide evidence for sulfate adsorption, or more accurately co-adsorption of water and (bi)sulfate ions, forming superstructures on the electrode surfaces. Our XAS measurements on Au electrodes (Fig. S6) confirm the occurrence of sulfate adsorption and the concomitant accumulation of H_3O^+ at the Au-H_2SO_4(aq) interface.

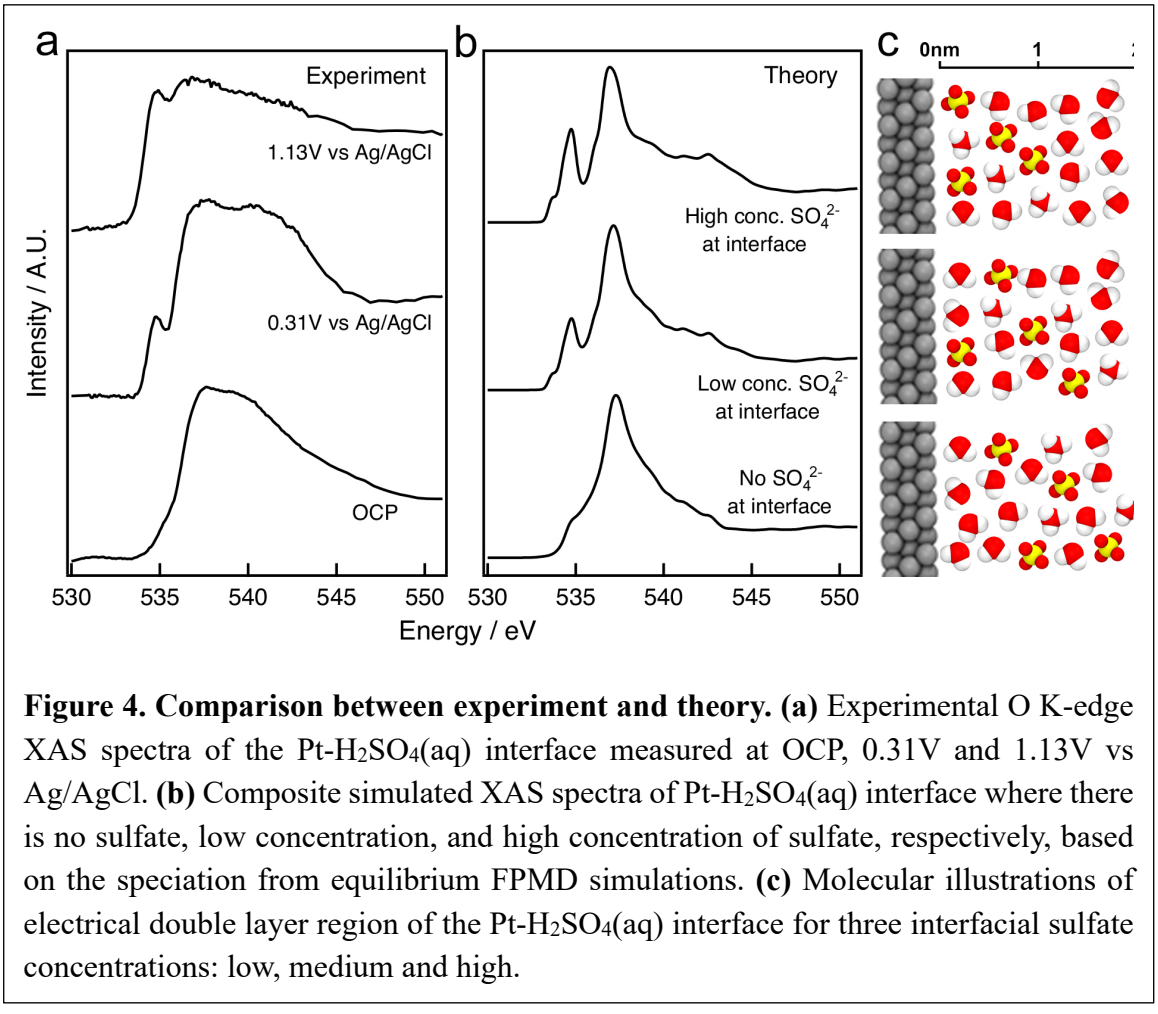

Figure 4. Comparison between experiment and theory. (a) Experimental O K-edge XAS spectra of the Pt-H_2SO_4(aq) interface measured at OCP, 0.31V and 1.13V vs Ag/AgCl. **(b)** Composite simulated XAS spectra of Pt-H_2SO_4(aq) interface where there is no sulfate, low concentration, and high concentration of sulfate, respectively, based on the speciation from equilibrium FPMD simulations. **(c)** Molecular illustrations of electrical double layer region of the Pt-H_2SO_4(aq) interface for three interfacial sulfate concentrations: low, medium and high.

The differences between the conclusions from our XAS results and those from other electrochemical studies may arise from the fact that our XAS measurements are performed while holding the voltage steady during the data acquisition at each voltage for about 20 minutes. As a result, our results more closely report the thermodynamic equilibrium structure at that voltage. This is fundamentally different from the transient, rate-dependent CV measurements, which probe the slow dynamics of physical or chemical transformations.

4. Conclusions

Using interface-sensitive *operando* EY-XAS, together with MD simulations, continuum modelling and XAS simulations, we could determine the chemical structure and speciation in the electric double layer at the Pt-H_2SO_4(aq) interface in the potential range above the hydrogen evolution and below the oxygen evolution reactions. We have demonstrated that for positive electrode potentials, the surface is decorated with sulfate (SO_4^{2-}) ions with nearby H_3O^+ in the first few layers (depending on the voltage) with no appreciable contribution of bisulfate or sulfuric acid (HSO_4^-, H_2SO_4). We have also shown that Pt-O/Pt-OH does not form at least up to 1.3V. In addition to a more complete determination of the EDL structure and composition, our study demonstrates the power of surface sensitive and element specific EY-XAS experiments combined with first-principles theory to probe the structure of buried, solid-liquid, functional electrochemical interfaces with molecular-scale detail. It solidifies the connections between time- and ensemble-averaged XAS measurements and the underlying thermodynamic mechanism for adsorption of species from the electrolyte to the electrode surface. These results open the way for future atomistic studies of the chemistry of interfaces relevant to electrochemistry and its applications to electrolysis, fuel cells, and energy storage, from batteries to supercapacitors.

Associate Content

Supporting Information. More details regarding materials and thin film preparation, experimental configuration of *operando* XAS measurements, XAS spectra analysis, saturation effects, FPMD and XAS spectra simulations, modeling of biased interfaces using continuum models, and supporting figures S1-S15. This material is available free of charge via the Internet at http://pubs.acs.org.

Author Information

Corresponding Author

M. B. Salmeron: mbsalmeron@lbl.gov

Author Contribution

‡ These authors contributed equally.

Acknowledgements

This work was supported by the Office of Basic Energy Sciences (BES), Division of Materials Sciences and Engineering, of the U.S. Department of Energy (DOE) under Contract No. DE-AC02-05CH11231, through the Structure and Dynamics of Materials Interfaces program (FWP KC31SM). The x-ray absorption spectroscopy measurements were performed at the Advanced Light Source, supported by DOE under the same contract. Theory and simulations were performed within a user project at the Molecular Foundry, Lawrence Berkeley National Laboratory, supported by the DOE under the same contract number. All computations are performed using the computing resources of the National Energy Research Scientific Computing Center (NERSC), supported by the Office of Science of the U.S. Department of Energy under the same contract. We also thank Dr. C. Das Pemmaraju, Dr. Liwen Wang, Dr. Craig Schwartz, Prof. Rich Saykally, Dr. Phil Ross, Prof. Xiaofeng Feng, and Dr. Steve Harris for useful discussions.

Notes

The authors declare no competing financial interest.

References

(1) Bard, A. J.; Abruna, H. D.; Chidsey, C. E.; Faulkner, L. R.; Feldberg, S. W.; Itaya, K.; Majda, M.; Melroy, O.; Murray, R. W. *J. Phys. Chem.* **1993**, *97*, 7147–7173.

(2) Bard, A. J.; Faulkner, L. R. *Electrochemical Methods: Fundamentals and Applications*; Wiley, 1980.

(3) Wu, C. H.; Weatherup, R. S.; Salmeron, M. B. *Phys. Chem. Chem. Phys.* **2015**, *17*, 30229–30239.

(4) Angerstein-Kozlowska, H.; Conway, B. E.; Sharp, W. B. A. *J. Electroanal. Chem. Interfacial Electrochem.* **1973**, *43*, 9–36.

(5) Conway, B. E.; Gottesfeld, S. *J. Chem. Soc. Faraday Trans. 1 Phys. Chem. Condens. Phases* **1973**, *69*, 1090.

(6) Tilak, B. V.; Conway, B. E.; Angerstein-Kozlowska, H. *J. Electroanal. Chem. Interfacial Electrochem.* **1973**, *48*, 1–23.

(7) Kolics, A.; Wieckowski, A. *J. Phys. Chem. B* **2001**, *105*, 2588–2595.

(8) Gamboa-Aldeco, M. E.; Herrero, E.; Zelenay, P. S.; Wieckowski, A. *J. Electroanal. Chem.* **1993**, *348*, 451–457.

(9) Wieckowski, A.; Kolics, A. *J. Electroanal. Chem.* **1999**, *464*, 118–122.

(10) Jerkiewicz, G.; Vatankhah, G.; Lessard, J.; Soriaga, M. P.; Park, Y. S. *Electrochim. Acta* **2004**, *49*, 1451–1459.

(11) Kongkanand, A.; Ziegelbauer, J. M. *J. Phys. Chem. C* **2012**, *116*, 3684–3693.

(12) Kim, J.; Urchaga, P.; Baranton, S.; Coutanceau, C.; Jerkiewicz, G. *Phys. Chem. Chem. Phys.* **2017**, *19*, 21955–21963.

(13) Kolb, D. M. *Angew. Chemie - Int. Ed.* **2001**, *40*, 1162–1181.

(14) Shen, Y. R.; Ostroverkhov, V. *Chem. Rev.* **2006**, *106*, 1140–1154.

(15) Osawa, M.; Tsushima, M.; Mogami, H.; Samjeské, G.; Yamakata, A. *J. Phys. Chem. C* **2008**, *112*, 4248–4256.

(16) Braunschweig, B.; Mukherjee, P.; Dlott, D. D.; Wieckowski, A. *J. Am. Chem. Soc.* **2010**, *132*, 14036–14038.

(17) Toney, M. F.; Howard, J. N.; Richer, J.; Borges, G. L.; Gordon, J. G.; Melroy, O. R.; Wiesler, D. G.; Yee, D.; Sorensen, L. B. *Nature* **1994**, *368*, 444.

(18) Nagy, Z.; You, H. *Electrochim. Acta* **2002**, *47*, 3037–3055.

(19) Climent, V.; Feliu, J. M. *J. Solid State Electrochem.* **2011**, *15*, 1297–1315.

(20) Markovic, N.; Schmidt, T. J.; Marković, N. M.; Schmidt, T. J.; Stamenković, V.; Ross, P. N. *Fuel Cells* **2001**, *1*, 105–116.

(21) Braunschweig, B.; Daum, W. *Langmuir* **2009**, *25*, 11112–11120.

(22) Jerkiewicz, G. *Prog. Surf. Sci.* **1998**, *57*, 137–186.

(23) Kunimatsu, K.; Samant, M. G.; Seki, H. *J. Electroanal. Chem. Interfacial Electrochem.* **1989**, *258*, 163–177.

(24) Savich, W.; Sun, S.-G.; Lipkowski, J.; Wieckowski, A. *J. Electroanal. Chem.* **1995**,

388, 233–237.
(25) Kunimatsu, K.; Samant, M. G.; Seki, H.; Philpott, M. R. *J. Electroanal. Chem. Interfacial Electrochem.* **1988**, *243*, 203–208.
(26) Markovic, N. M.; Ross Jr., P. N. *Surf. Sci. Rep.* **2002**, *45*, 117–229.
(27) Redmond, E. L.; Setzler, B. P.; Alamgir, F. M.; Fuller, T. F. *Phys. Chem. Chem. Phys.* **2014**, *16*, 5301–5311.
(28) Teliska, M.; O'Grady, W. E.; Ramaker, D. E. *J. Phys. Chem. B* **2005**, *109*, 8076–8084.
(29) Faguy, P. W.; Marinković, N. S.; Adžić, R. R. *J. Electroanal. Chem.* **1996**, *407*, 209–218.
(30) Sawatari, Y.; Inukai, J.; Ito, M. *J. Electron Spectros. Relat. Phenomena* **1993**, *64–65*, 515–522.
(31) Kunimatsu, K.; Samant, M. G.; Seki, H. *J. Electroanal. Chem.* **1989**, *272*, 185–194.
(32) Lachenwitzer, A.; Li, N.; Lipkowski, J. *J. Electroanal. Chem.* **2002**, *532*, 85–98.
(33) Velasco-Velez, J. J.; Wu, C. H.; Pascal, T. A.; Wan, L. F.; Guo, J.; Prendergast, D.; Salmeron, M. *Science* **2014**, *346*, 831–834.
(34) Zheng, H.; Meng, Y. S.; Zhu, Y. *MRS Bull.* **2015**, *40*, 12–18.
(35) Nemšák, S.; Shavorskiy, A.; Karslioglu, O.; Zegkinoglou, I.; Rattanachata, A.; Conlon, C. S.; Keqi, A.; Greene, P. K.; Burks, E. C.; Salmassi, F.; Gullikson, E. M.; Yang, S.-H.; Liu, K.; Bluhm, H.; Fadley, C. S. *Nat. Commun.* **2014**, *5*, 5441.
(36) Axnanda, S.; Crumlin, E. J.; Mao, B.; Rani, S.; Chang, R.; Karlsson, P. G.; Edwards, M. O. M.; Lundqvist, M.; Moberg, R.; Ross, P.; Hussain, Z.; Liu, Z. *Sci. Rep.* **2015**, *5*, 9788.
(37) Kumar, S.; Bouzida, D.; Swendsen, R. H.; Kollman, P. A.; Rosenberg, J. M. *J. Comput. Chem.* **1992**, *13*, 1011–1021.
(38) Torrie, G. M.; Valleau, J. P. *J. Comput. Phys.* **1977**, *23*, 187–199.
(39) Baskin, A.; Prendergast, D. *J. Electrochem. Soc.* **2017**, *164*, E3438–E3447.
(40) Prendergast, D.; Galli, G. *Phys. Rev. Lett.* **2006**, *96*, 215502.
(41) England, A. H.; Duffin, A. M.; Schwartz, C. P.; Uejio, J. S.; Prendergast, D.; Saykally, R. J. *Chem. Phys. Lett.* **2011**, *514*, 187–195.
(42) Ramaswamy, N.; Mukerjee, S. *Adv. Phys. Chem.* **2012**, *2012*, 1–17.
(43) Nilsson, A.; Nordlund, D.; Waluyo, I.; Huang, N.; Ogasawara, H.; Kaya, S.; Bergmann, U.; Näslund, L.-Å.; Öström, H.; Wernet, P.; Andersson, K. J.; Schiros, T.; Pettersson, L. G. M. *J. Electron Spectros. Relat. Phenomena* **2010**, *177*, 99–129.
(44) Comas-Vives, A.; Bandlow, J.; Jacob, T. *Phys. Chem. Chem. Phys.* **2013**, *15*, 992–997.
(45) Kim, Y. G.; Soriaga, J. B.; Vigh, G.; Soriaga, M. P. *J. Colloid Interface Sci.* **2000**,

227, 505–509.
(46) Luzar, A.; Chandler, D. *Nature* **1996**, *379*, 55.
(47) Miller, D. J.; Öberg, H.; Kaya, S.; Sanchez Casalongue, H.; Friebel, D.; Anniyev, T.; Ogasawara, H.; Bluhm, H.; Pettersson, L. G. M.; Nilsson, a. *Phys. Rev. Lett.* **2011**, *107*, 195502.

TOC Graph

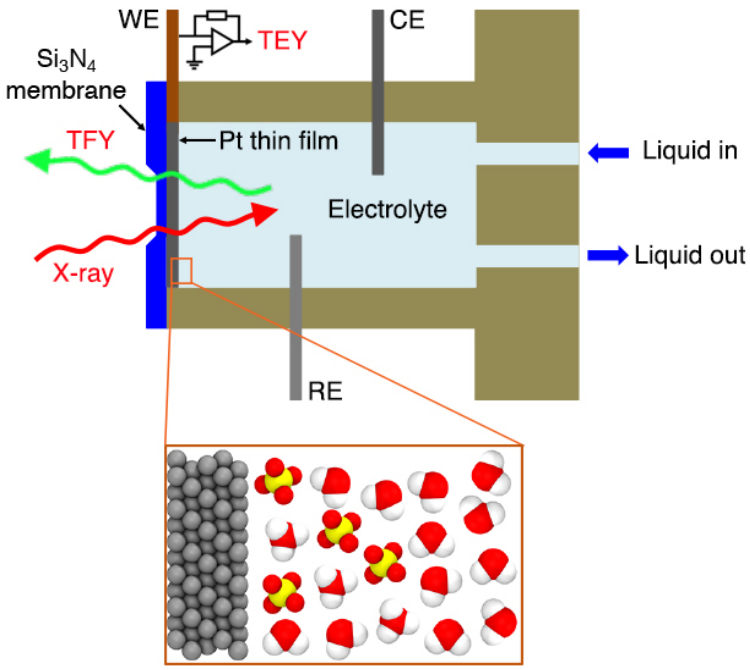
WE
TEY
CE
Si_3N_4
membrane
TFY
Pt thin film
Liquid in
Electrolyte
Liquid out
X-ray
RE

Supplementary Information for

The molecular scale structure of electrode-electrolyte interfaces: the case of platinum-sulfuric acid solution

Cheng Hao Wu[1,2,§], Tod A. Pascal[3,§], Artem Baskin[3], Huixin Wang[2,4], Hai-Tao Fang[2,4], Yi-Sheng Liu[5], Yi-Hsien Lu[2], Jinghua Guo[5,6], David Prendergast[3], and Miquel B. Salmeron[2,7,*]

[1] *Department of Chemistry, University of California, Berkeley, Berkeley CA, USA*

[2] *Materials Science Division, Lawrence Berkeley National Laboratory, Berkeley CA, USA*

[3] *The Molecular Foundry, Lawrence Berkeley National Laboratory, Berkeley CA, USA*

[4] *School of Materials Science and Engineering, Harbin Institute of Technology, Harbin, P. R. China*

[5] *The Advanced Light Source, Lawrence Berkeley National Laboratory, Berkeley CA, USA*

[6] *Department of Chemistry and Chemical Biology, University of California, Santa Cruz, Santa Cruz CA, USA*

[7] *Department of Materials Science and Engineering, University of California, Berkeley, Berkeley CA, USA*

§These authors contributed equally to this work

*Corresponding Email: mbsalmeron@lbl.gov

Methods

1. Materials and thin film preparation

Standard 0.1N (0.05M) sulfuric acid solution was purchased from Sigma-Aldrich and used without any purification or other treatment. The Pt (or Au) thin film (15 nm) was evaporated onto the flat side of the Si_3N_4 window by an e-beam evaporator under 10^{-8} Torr base pressure. A thin Ti layer (2 nm) was deposited prior to the Pt deposition to achieve better adhesion between Pt and Si_3N_4 membrane. The Ti adhesion layer is fully covered by platinum and no TiO_2 signature could be seen in all the O K-edge TEY-XAS spectrum acquired.

2. Experiment configurations of *operando* XAS measurements

The *operando* XAS experiments were performed at beamline 8.0.1.3 (Wet-RIXS) endstation of the Advanced Light Source, the synchrotron facility at Lawrence Berkeley National Laboratory.

As previously described[1] and illustrated in Fig. S1, the Si_3N_4 window covered with Pt or Au thin film was assembled in a flow liquid cell, containing a Pt wire and a miniature Ag/AgCl electrode as counter electrode (CE) and reference electrodes (RE), respectively. During *operando* XAS measurements, the bias was applied between the working electrode (WE), i.e. the Pt thin film or Au thin film, and the Pt CE, and the voltage was provided by the SRS570 pre-amplifier bias output function. The reported potentials with respect to the Ag/AgCl RE, were the average values of potential difference between WE and RE measured before and after the acquisition of each spectrum under x-ray illumination. At potentials above open circuit potential (OCP), the total drift in potential with respect to the RE is small (<50mV) during the data acquisition time of each spectrum (~20min). At potentials below OCP however, the drift becomes larger and the quality of the EY-XAS signal becomes noticeably worse, as illustrated in Fig. S6.

We should note that x-ray illumination of the WE induced a potential drop of ~ 0.3V relative to RE, because of the extra (secondary electron) current induced by x-ray illumination. At low current conditions (such as OCP), the small TEY current (typically 1-10nA) will lead to re-equilibration between WE and CE and thus the shift in measured potential relative to RE. This is why our OCP potentials are approximately 0.3V more negative than the values commonly reported in the literature (0.5-0.6V vs Ag/AgCl). But when the ionic current is large (e.g. around the anodic or cathodic peaks), such small

current is negligible; as a result, its impact on relative potentials is very small. Overall, we did not observe shifts or distortions in the CV profile under x-ray illumination. For the sake of consistency, all the potentials relative to RE reported in this study were recorded under x-ray illumination. Although it is feasible to conduct three-electrode constant potential amperometry in the liquid cell using a commercial potentiostat, such configuration introduces a much higher level of noise during collection of EY signal. The two-electrode configuration introduces substantially less noise and generates reproducible data. The bias applied between WE and CE were limited within the ±1.3V window to avoid substantial water electrolysis reactions, which will produce large volume of gases leading to pressure build-up and rupture of the Si_3N_4 window.

Total fluorescence yield (TFY) XAS spectra were collected simultaneously with EY-XAS during each measurement, using a negatively biased channeltron detector. Because TFY-XAS measures the photons emitted after x-ray excitation, whose mean free path in liquids is on the order of μm, TFY-XAS is therefore a bulk-sensitive measurement in comparison with surface- or interface-sensitive EY-XAS.

3. XAS spectra analysis

For each of the raw XAS spectrum, the intensity was first normalized by the photon flux, represented by the TEY current from a gold mesh installed upstream in the x-ray pipeline. A straight-line background was subtracted from the flux-normalized spectrum based on the linear fit of the flat region before the absorption edge. All the spectra were normalized again by setting the intensity of the flat tail (between 550 and 560 eV) to unity.

Numerical fitting was performed in some of the XAS spectra using four Gaussian components after subtraction of an arctan background. The purpose of such fitting was to quantitatively compare the width of the pre-peaks at 535 eV, without attempt to determine the exact physical origin of each component.

4. Saturation effects

As pointed out in the main text, the O K-edge spectra acquired at the most positive potentials (>1V vs Ag/AgCl) exhibit long flat tails, reminiscent of bulk water XAS spectra that suffer from saturation effects. Such effect is typically seen in the fluorescence yield (FY) XAS but not in electron yield (EY) XAS, with the exception of low-energy partial electron yield (PEY), as demonstrated by Nilsson et al.[2] where secondary electrons

with very low kinetic energy (<20eV) are filtered and collected via a biased electrode. Because the mean free path of these low energy electrons can be comparable to that of soft x-ray photons, such PEY XAS measurements can suffer from saturation effects.

While an increase in current due to low energy secondary electrons originating deeper in the solution and attracted to the positive electrode voltage seems plausible in principle, one should also consider the countering effect of screening of the electrode potential by the electrical double layer. Although these effects are not yet fully understood, we believe that saturation effects are not severe enough here to substantially distort the EY-XAS spectra, at least for positive bias below ~1V. Indeed, the lack of pre-edge features (related to broken hydrogen bonds) in the XAS spectra collected at OCP indicates that these low energy electrons can only account for a very small portion of the electrons collected in the EY-XAS measurements because otherwise the EY-XAS spectrum would resemble the saturated spectrum of bulk water with strong pre-peak at 535eV. One would also expect saturated bulk water spectra at positive bias no matter what solute in the aqueous solution. The fact that we obtain different potential-dependence XAS under positive potentials for both Au-H_2O and Au/Pt-H_2SO_4(aq) interfaces suggests that this is not the case.

5. First Principles Molecular Dynamics (FPMD) Simulations

We used a system comprising a Pt electrode (represented by a 4×4×6 supercell of the fundamental unit cell containing 96 Pt atoms in total, with the (111) surface exposed and a surface area of 1.12×0.97 nm^2), 119 water molecules, and various amounts of $H_2SO_4/HSO_4^-/SO_4^{2-}$ molecules with the corresponding amount of H_3O^+ molecules to achieve overall neutrality in the system. Surface coverages ranging from 0.083 (1 sulfate species) to 0.83 (10 sulfate species) were considered.

We first equilibrated each system by performing 25ps constant volume, constant temperature (canonical or NVT ensemble) FPMD simulations at 350K within density functional theory (DFT). We employed a modified version of the mixed Gaussian and plane wave code[3] CP2K/Quickstep.[4] The electronic structure of the atoms was described using a triple-ζ basis set with two additional sets of polarization functions (TZV2P)[5] and a 320 Ry plane-wave cutoff. We used the Perdew-Burke-Ernzerhof (PBE) form of the generalized-gradient approximation of the unknown exchange-correlation potential in DFT,[6] and the Brillouin zone is sampled at the Γ-point only. Interactions between the valence electrons and the ionic cores are described by norm-conserving

pseudopotentials.[7,8] The Poisson equation is solved using an efficient Wavelet-based solver.[9] We overcome the poor description of the short-range dispersive forces within the PBE-GGA exchange-correlation functional by employing the DFTD3 empirical corrections of Grimme et al.[10] Snapshots of the system were saved at every step. We recognize that particular chemical species near the interface can efficiently change identity via exchange of protons through surrounding water molecules and that there is a known overestimation of the rate of dissociation of bisulfate (HSO_4^- + H_2O ⇔ H_3O^+ + SO_4^{2}) in the bulk phase when employing the generalized-gradient approximation within DFT-based FPMD.[11] Therefore when performing FPMD simulations we impose fixed speciation by restricting the number of protons associated to each molecule through a constraint on the coordination number.

After equilibration, the binding free energy of a randomly selected sulfate molecule to the platinum electrode was separately obtained from umbrella sampling[12] calculations, employing the center of mass distances as the collective variable. In other words, we introduced a reaction coordinate ξ and defined a harmonic umbrella potential function V(ξ(r)) in the following form:

$$V\left(\xi\left(r\right)\right) = k\left(\xi\left(r\right) - r_0\right)^2$$

where k is the force constant [10 kcal/(mol Å^2)], and r_0 is the equilibrium distance. We used a simulation time step of 0.5fs. Separate simulations were run, with biased potentials centered along the reaction coordinate in 20 windows, with 0.5Å displacements from 0 to 1nm. We verified that these simulations parameters yielded overlapping Gaussian distributions at various r_0 distances. At each displacement, we carried out 5ps NVT dynamics, with the system coordinates saved every 10fs. The free energy of binding was subsequently obtained from the potential of mean force, calculated using the weighted histogram analysis method,[13,14] with a convergence tolerance of 1×10^{-4} kcal/mol. We ignored the first 1ps of dynamics at each window when calculating the free energy.

6. XAS spectra simulations

During the last 10ps of NVT FPMD equilibrium simulation, snapshots of the atomic positions of the system were saved every 0.5ps (a total of 20 snapshots for each system), and used as input for an in-house code employing constrained-occupancy DFT calculations within the XCH approximation[15–17] to calculate the XAS spectra. Plane-wave pseudopotential calculations using ultrasoft pseudopotentials[18] were performed using the

PWSCF code within the Quantum-ESPRESSO package.[19] We used a kinetic energy cut-off for electronic wave functions of 25 Ry and a density cut-off of 200 Ry. The core-excited Kohn-Sham eigenspectrum was generated using the XCH approach.[17] Based on a numerically converged self-consistent charge density, we generated the unoccupied states for our XAS calculations non-self-consistently by sampling the first Brillouin zone at the Γ-point, employing an implementation of the Shirley interpolation scheme[20] generalized to handle ultra-soft pseudopotentials.[21] Matrix elements were evaluated within the PAW frozen-core approximation.[22] Core-excited ultrasoft pseudopotentials and corresponding atomic orbitals were generated with the Vanderbilt code.[18] Each computed transition was convoluted with a 0.2 eV Gaussian function to produce continuous spectra.

Because of the use of pseudopotentials we can only reliably compare the calculated relative excitation energies. We used an alignment scheme based on energy differences between ground and core-excited states of the system and those of an isolated atom in the same simulation cell.[16,23] Direct comparison to experiment is accomplished by first calibrating an unambiguous reference system. In the case of the oxygen compounds considered in this study, we rigidly shifted the first major peak in the oxygen K-edge XAS of an isolated CO_2 molecule by +526.9 eV to match the same in a gas phase experiment.[24] This empirical shift, is unique to the pseudopotentials employed in this study, and is applied to all subsequent calculated spectra. Previous experience has shown that this alignment scheme predicts XAS peak positions to within ~0.1 eV,[15,16] which is close to the experimental uncertainty in this energy range. It is well know that Kohn-Sham DFT within the PBE approximation underestimates band gaps[25,26] and concomitantly band-widths due to inaccurate quasiparticle (excitation) energies.[27,28] As a result, the calculated XAS spectrum is usually too narrow compared to experiments. We thus dilated the computed XAS spectrum by 20%, as in previous work.[29–31]

7. Modeling of Biased Interfaces using Continuum Models

In the modeling of biased interfaces using continuum models we assumed that in the thermodynamic equilibrium the ion concentration profiles account for the relaxation of electrostatic forces and that interconversion of ions is governed by equilibrium constants K_1 and K_2. The self-consistent solutions of the corresponding generalized Poisson-Boltzmann equation provided the complementary picture of speciation at biased Pt-electrode interfaces.

7.1 General formalism

To build the continuum model including three types of ions (sulfate, bisulfate, and hydronium), all of which have finite size and can specifically adsorb on electrode surface except hydronium, we used the free energy functional that has the following form:[32]

$$\Omega[\varphi(\vec{r});\rho_{\pm}(r)] = \int d\vec{r}\left\{-\frac{\varepsilon(\vec{r})}{8\pi}|\nabla\varphi|^2 + e\varphi(\rho_+ - \rho_{1-} - \rho_{2-}) + \Phi_1(\vec{r})\rho_{1-} + \Phi_2(\vec{r})\rho_+ + \Phi_3(\vec{r})\rho_{2-} - \mu_{1-}\rho_{1-} - \mu_{2-}\rho_{2-} - \mu_+\rho_+\right\} + \frac{k_BT}{a^3}\int d\vec{r}\{a^3\rho_{1-}\ln a^3\rho_{1-} + a^3\rho_{2-}\ln a^3\rho_{2-} + a^3\rho_+\ln a^3\rho_+ + (1 - a^3\rho_{1-} - a^3\rho_{2-} - a^3\rho_+)\ln(1 - a^3\rho_{1-} - a^3\rho_{2-} - a^3\rho_+)\}.$$

The Poisson-Boltzmann equation, as well as concentration profiles for ions, were obtained via the variational method:

$$\nabla(\varepsilon(\vec{r})\nabla\varphi) = -4\pi e\left(\rho_+ - \rho_{1-} - 2\rho_{2-}\right)$$

with boundary conditions $\frac{\partial\varphi}{\partial z}|_{z\to\infty} = 0$, $\frac{\partial\varphi}{\partial z}|_{z\to 0} = -\frac{\sigma}{\varepsilon_0\varepsilon}$, where σ is the surface charge density.

7.2 Input parameters

In this approximation the size of all ions was set equally to 6Å. Such simplification would slightly underestimate the concentration of hydronium ions because their actual size is smaller than that of (bi)sulfate ions. The overall surface coverage by ions would be overestimated since we did not consider the solvent (water) molecules explicitly.

To reflect the inhomogeneity in dielectric response of water near the surface, we used a spatially dependent dielectric function that has the following form:

$$\varepsilon(z) = 1 + \frac{\varepsilon - 1}{1 + exp\left(-\alpha\left(z - z_0'\right)\right)},$$

where ε = 78.3, α = 4 Å^{-1}, and z_0' = 2.8 Å.

The adsorption potentials $\Phi_{1,2,3}(\vec{r})$ were adapted from the FPMD free energy calculations (Fig. S9a) and then renormalized by Coulombic potentials of the image charge interaction (the interaction of a point charge with an ideal metal surface in the media with

inhomogeneous dielectric function $\varepsilon(z)$ as defined earlier), as the first term in the Green's function of equation $\nabla(\varepsilon(z)\nabla\varphi) = -4\pi\delta(r - \vec{r}')$. The normalization terms generally have the following forms:

$$U(z)[eV] = -\frac{3.6\,\alpha^2}{\varepsilon(z)z[\text{Å}]},$$

where α is the charge on the ion.

The resulting potentials were then approximated with Morse potentials:

$$\Phi(z) = E_{ads}\left(1 - e^{-k(z-z_0)}\right)^2 - E_{ads}.$$

The adsorption energy E_{ads} is 0.12 eV for sulfate ions and 0.14 eV for bisulfate, which reflects the higher penalty for de-solvation of divalent ion (11.3 eV) as compared to monovalent (3.2 eV).[33] The slope parameter k was set to 4 and z_0 = 2.7Å. For hydronium ions we assume no specific adsorption by imposing a repulsion wall at z = 2.2Å.

We used the equilibrium constants reported in the literature[34] (K_1=1000, K_2=0.0102) to calculate the bulk equilibrium concentrations of ions. In a 0.05M H_2SO_4 solution, the equilibrium concentrations of sulfate, bisulfate, and hydronium ions are calculated to be 0.0075, 0.042, and 0.057M, respectively. Based on the thermodynamic cycle illustrated in Fig. S10, the equilibrium constant for adsorbed (bi)sulfate ions needs to be modified as follows:

$$K_2' = K_2 \frac{K_{ads}^{SO_4^{2-}}}{K_{ads}^{HSO_4^-}}.$$

Based on our FPMD simulations, the adsorption free energy of sulfate and bisulfate ions are almost equal (Fig. S9a) and therefore $K_2' \approx K_2$.

7.3 Self-consistent solutions

We used the scheme illustrated in Fig. S11 to obtain the equilibrium distribution of ions near the electrified surface. The results are shown in Fig. S12 where we compare the profiles with and without an additional equilibration based on the equilibrium constants K_1, K_2'. As one can see, at sufficiently positive potentials sulfate ions dominate in the interfacial region.

We also obtained the surface excess of ions as a function of surface charge density (Fig. S13a), and electrode potential (Fig. S13b), by integrating the ion concentration profiles over the interfacial regions at a given surface charge density or electrode potential. The results shown in Fig. 13 clearly showed co-adsorption of bisulfate ions and sulfate ions dominate in the interfacial region at potentials above 0.1V. The asymmetry of the curves arises from the differences in adsorption potentials and the charges between hydronium and (bi)sulfate ions.

References

(1) Velasco-Velez, J. J.; Wu, C. H.; Pascal, T. A.; Wan, L. F.; Guo, J.; Prendergast, D.; Salmeron, M. *Science* **2014**, *346*, 831–834.

(2) Nilsson, A.; Nordlund, D.; Waluyo, I.; Huang, N.; Ogasawara, H.; Kaya, S.; Bergmann, U.; Näslund, L.-Å.; Öström, H.; Wernet, P.; Andersson, K. J.; Schiros, T.; Pettersson, L. G. M. *J. Electron Spectros. Relat. Phenomena* **2010**, *177*, 99–129.

(3) Lippert, G.; Hutter, J.; Parrinello, M. *Mol. Phys.* **1997**, *92*, 477–488.

(4) VandeVondele, J.; Krack, M.; Mohamed, F.; Parrinello, M.; Chassaing, T.; Hutter, J. *Comput. Phys. Commun.* **2005**, *167*, 103–128.

(5) VandeVondele, J.; Hutter, J. *J. Chem. Phys.* **2007**, *127*, 114105.

(6) Perdew, J. P.; Burke, K.; Ernzerhof, M. *Phys. Rev. Lett.* **1996**, *77*, 3865–3868.

(7) Goedecker, S.; Teter, M.; Hutter, J. *Phys. Rev. B* **1996**, *54*, 1703–1710.

(8) Krack, M. *Theor. Chem. Acc.* **2005**, *114*, 145–152.

(9) Genovese, L.; Deutsch, T.; Goedecker, S. *J. Chem. Phys.* **2007**, *127*, 54704.

(10) Grimme, S.; Antony, J.; Ehrlich, S.; Krieg, H. *J. Chem. Phys.* **2010**, *132*, 154104.

(11) Wan, Q.; Spanu, L.; Gygi, F.; Galli, G. *J. Phys. Chem. Lett.* **2014**, *5*, 2562–2567.

(12) Torrie, G. M.; Valleau, J. P. *J. Comput. Phys.* **1977**, *23*, 187–199.

(13) Grossfield, A. WHAM: an implementation of the weighted histogram analysis method, version 2.0.7, 2013.

(14) Chodera, J. D.; Swope, W. C.; Pitera, J. W.; Seok, C.; Dill, K. A. *J. Chem. Theory Comput.* **2007**, *3*, 26–41.

(15) Pascal, T. A.; Boesenberg, U.; Kostecki, R.; Richardson, T. J.; Weng, T.-C.; Sokaras, D.; Nordlund, D.; McDermott, E.; Moewes, A.; Cabana, J.; Prendergast, D. *J. Chem. Phys.* **2014**, *140*, 34107.

(16) England, A. H.; Duffin, A. M.; Schwartz, C. P.; Uejio, J. S.; Prendergast, D.; Saykally, R. J. *Chem. Phys. Lett.* **2011**, *514*, 187–195.

(17) Prendergast, D.; Galli, G. *Phys. Rev. Lett.* **2006**, *96*, 215502.

(18) Vanderbilt, D. *Phys. Rev. B* **1990**, *41*, 7892–7895.

(19) Giannozzi, P.; Baroni, S.; Bonini, N.; Calandra, M.; Car, R.; Cavazzoni, C.; Ceresoli, D.; Chiarotti, G. L.; Cococcioni, M.; Dabo, I.; Dal Corso, A.; de Gironcoli, S.; Fabris, S.; Fratesi, G.; Gebauer, R.; Gerstmann, U.; Gougoussis, C.; Kokalj, A.; Lazzeri, M.; Martin-Samos, L.; Marzari, N.; Mauri, F.; Mazzarello, R.; Paolini, S.; Pasquarello, A.; Paulatto, L.; Sbraccia, C.; Scandolo, S.; Sclauzero, G.; Seitsonen, A. P.; Smogunov, A.; Umari, P.; Wentzcovitch, R. M. *J. Phys. Condens. Matter* **2009**, *21*, 395502.
(20) Shirley, E. *Phys. Rev. B* **1996**, *54*, 464–469.
(21) Prendergast, D.; Louie, S. G. *Phys. Rev. B* **2009**, *80*, 235126.
(22) Taillefumier, M.; Cabaret, D.; Flank, A.-M. A.; Mauri, F. *Phys. Rev. B* **2002**, *66*, 1–11.
(23) Jiang, P.; Prendergast, D.; Borondics, F.; Porsgaard, S.; Giovanetti, L.; Pach, E.; Newberg, J.; Bluhm, H.; Besenbacher, F.; Salmeron, M. *J. Chem. Phys.* **2013**, *138*, 24704.
(24) Sham, T. K.; Yang, B. X.; Kirz, J.; Tse, J. S. *Phys. Rev. A* **1989**, *40*, 652–669.
(25) Cohen, A. J.; Mori-Sánchez, P.; Yang, W. *Phys. Rev. B* **2008**, *77*, 115123.
(26) Mori-Sánchez, P.; Cohen, A. J.; Yang, W. *Phys. Rev. Lett.* **2008**, *100*, 146401.
(27) Fuchs, F.; Furthmüller, J.; Bechstedt, F.; Shishkin, M.; Kresse, G. *Phys. Rev. B* **2007**, *76*, 115109.
(28) Aulbur, W. G.; Jönsson, L.; Wilkins, J. W. 2000; pp. 1–218.
(29) Pascal, T.; Wujcik, K.; Velasco-Velez, J.; Wu, C.; Teran, A.; Kapilashrami, M.; Cabana, J.; Guo, J.; Salmeron, M.; Balsara, N.; Prendergast, D. *J. Phys. Chem. Lett.* **2014**, *5*, 1547–1551.
(30) Pascal, T. A.; Pemmaraju, C. D.; Prendergast, D. *Phys. Chem. Chem. Phys.* **2015**, *17*, 7743–7753.
(31) Pascal, T. A.; Villaluenga, I.; Wujcik, K. H.; Devaux, D.; Jiang, X.; Wang, D. R.; Balsara, N.; Prendergast, D. *Nano Lett.* **2017**, *17*, 2517–2523.
(32) Baskin, A.; Prendergast, D. *J. Electrochem. Soc.* **2017**, *164*, E3438–E3447.
(33) Marcus, Y. *Chem. Rev.* **1988**, *88*, 1475–1498.
(34) Dawson, B. S. W.; Irish, D. E.; Toogood, G. E. *J. Phys. Chem.* **1986**, *90*, 334–341.

Supporting Figures

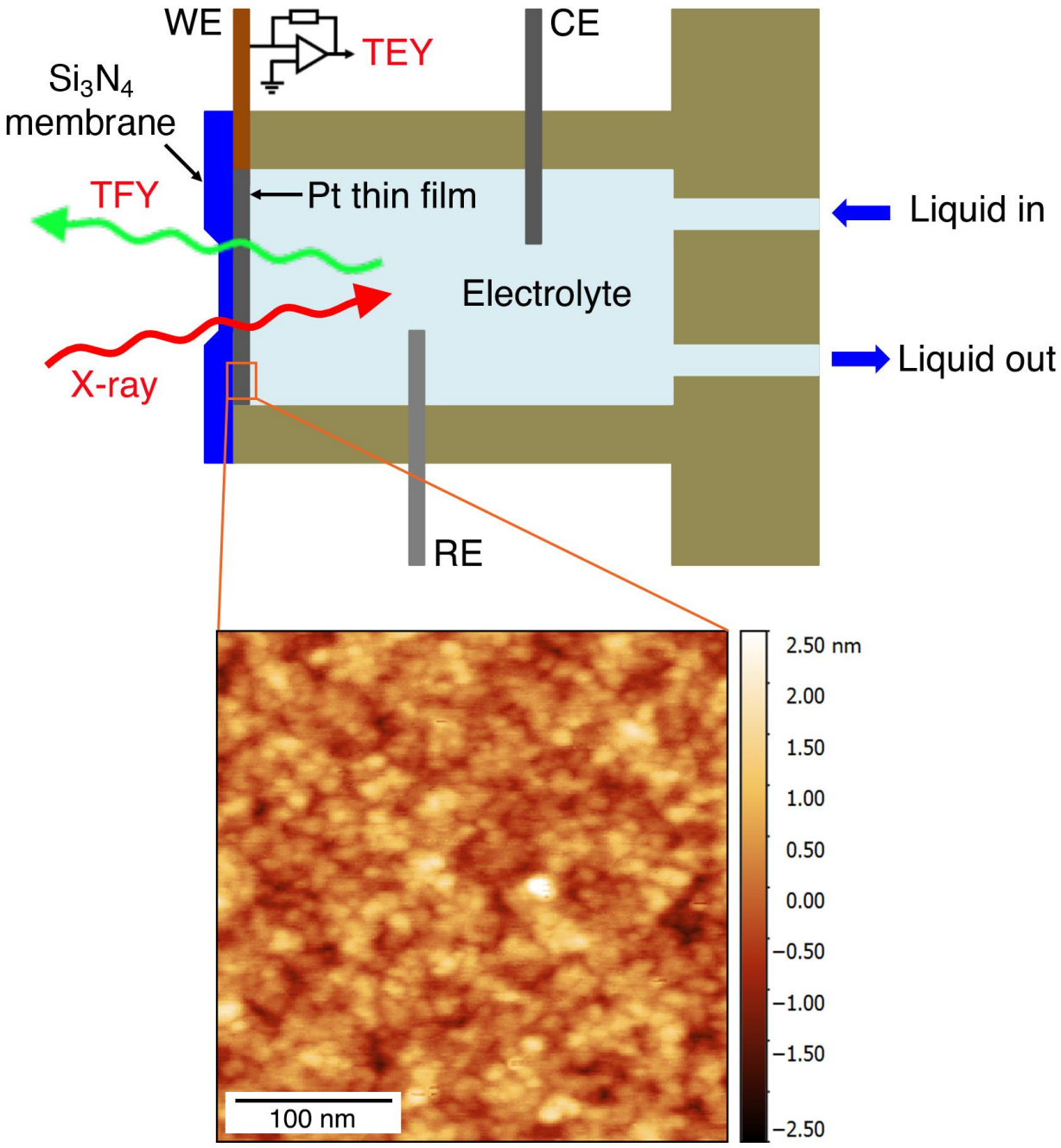

Figure S1. Schematics of the flow liquid cell and typical topological AFM Image of the evaporated Pt thin film (RMS roughness ~ 0.5nm).

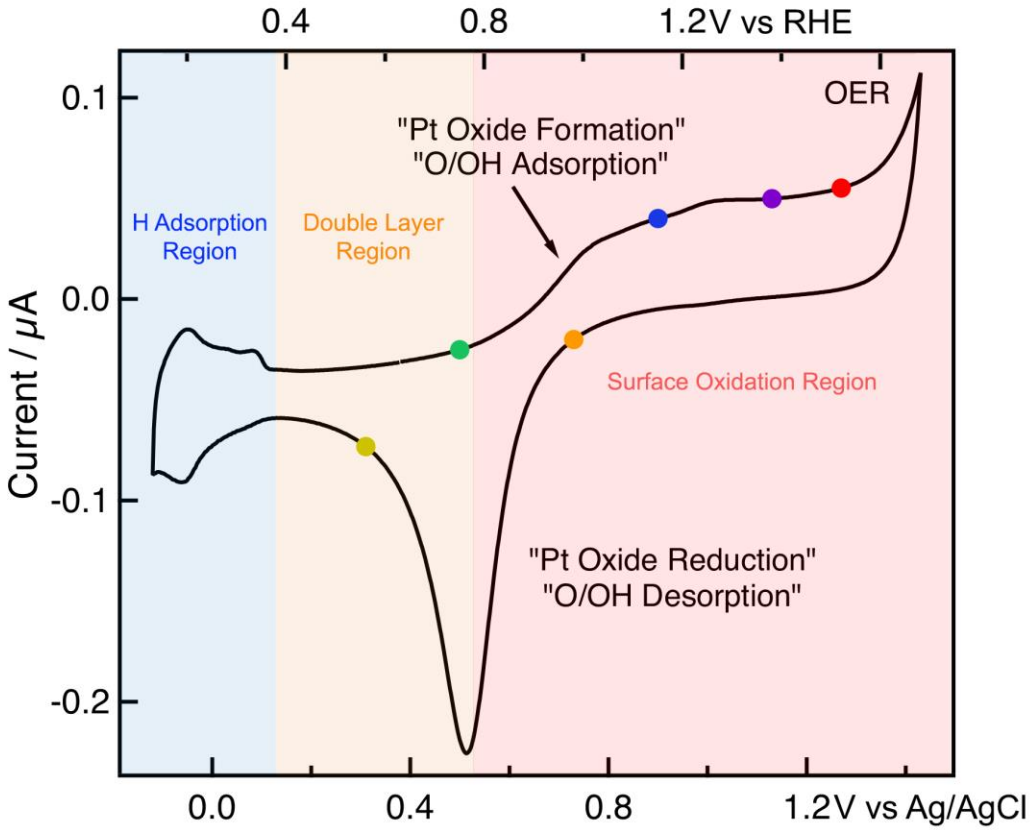

Figure S2. Typical CV curve of the thin film Pt electrode in 0.05M H_2SO_4 solution measured in the liquid cell with Pt CE and Ag/AgCl RE. The scan rate is 50mV/s. The curve was divided into three regions, each colored and labeled based on conventional models in the electrochemical literature. The potential scale with respect to RHE (assuming pH = 1) is shown at the top of the graph for reference.

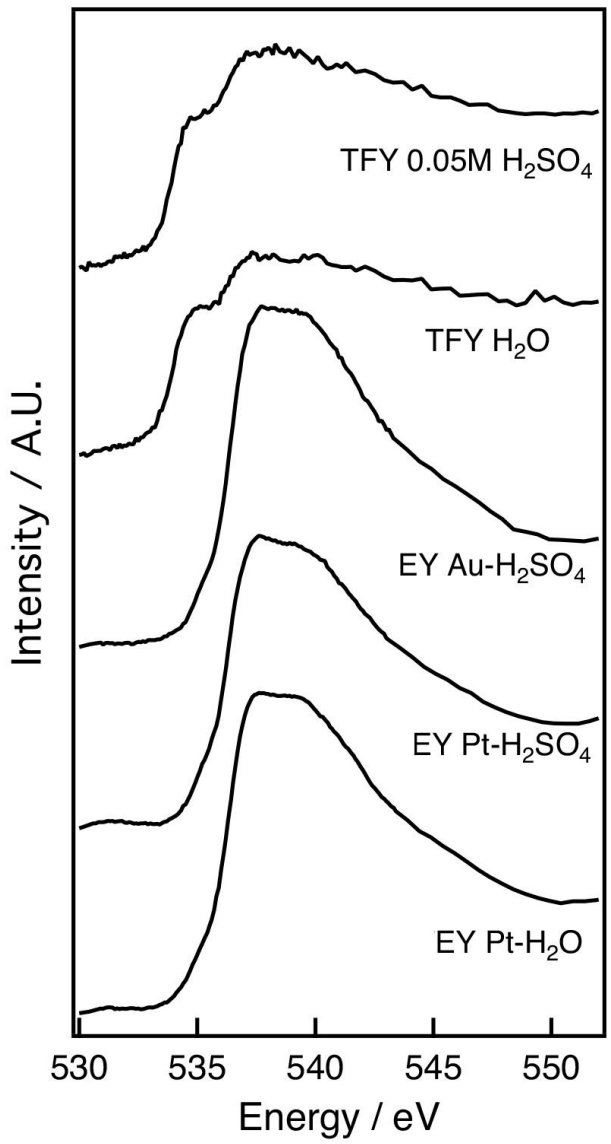

Figure S3. Comparison of O K-edge EY-XAS spectra under OCP at Au-H_2SO_4(aq), Pt-H_2SO_4(aq), Pt-H_2O interfaces and TFY-XAS spectra of pure H_2O and 0.05M H_2SO_4 solution.

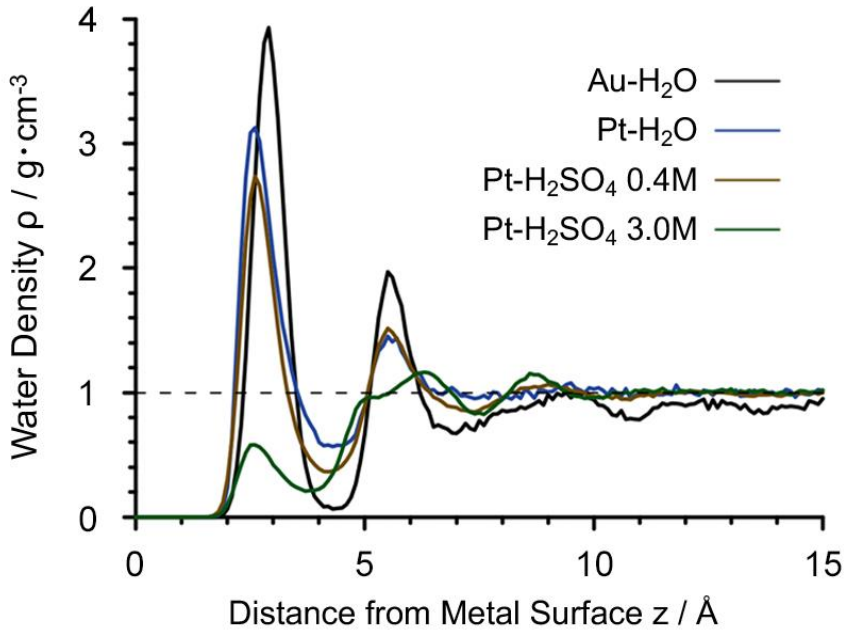

Figure S4: Water mass density distribution at various interfaces from FPMD simulations. The center of mass position of each water molecule is discretized in 0.1Å bins and averaged every 10fs over the last 10ps of the FPMD trajectory. Each distribution profile shows three structured water layers: the first molecular layer lies within 1.2-3.9Å with a peak maximum at ~3Å, the second interfacial layer lies at 3.9-6.6 Å from the surface, and a possible third layer at 6.6-9.4Å, after which the density converges to the bulk value.

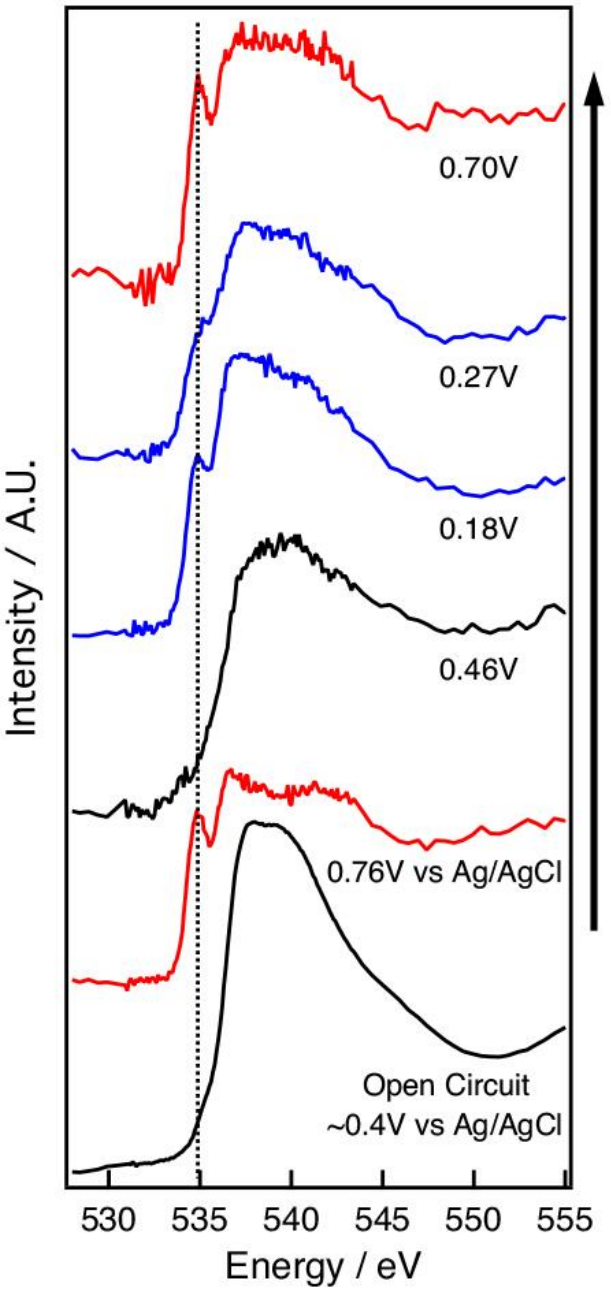

Figure S5. *Operando* O K-edge EY-XAS spectra of the Au-H_2SO_4(aq) interface at different potentials. The black arrow indicates the order of spectra acquisition.

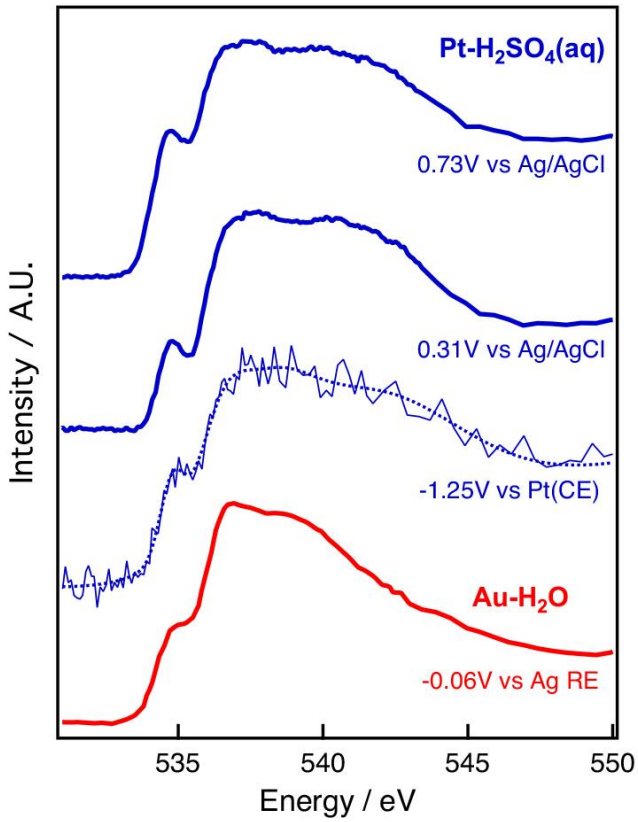

Figure S6. Comparison of O K-edge EY-XAS spectra collected at Pt-H_2SO_4(aq) interface at 0.73V and 0.31V vs Ag/AgCl and at -1.25V vs Pt CE, as well as EY-XAS spectrum at Au-H_2O interface at -0.06V vs Ag pseudo-reference electrode as previously reported.[1]

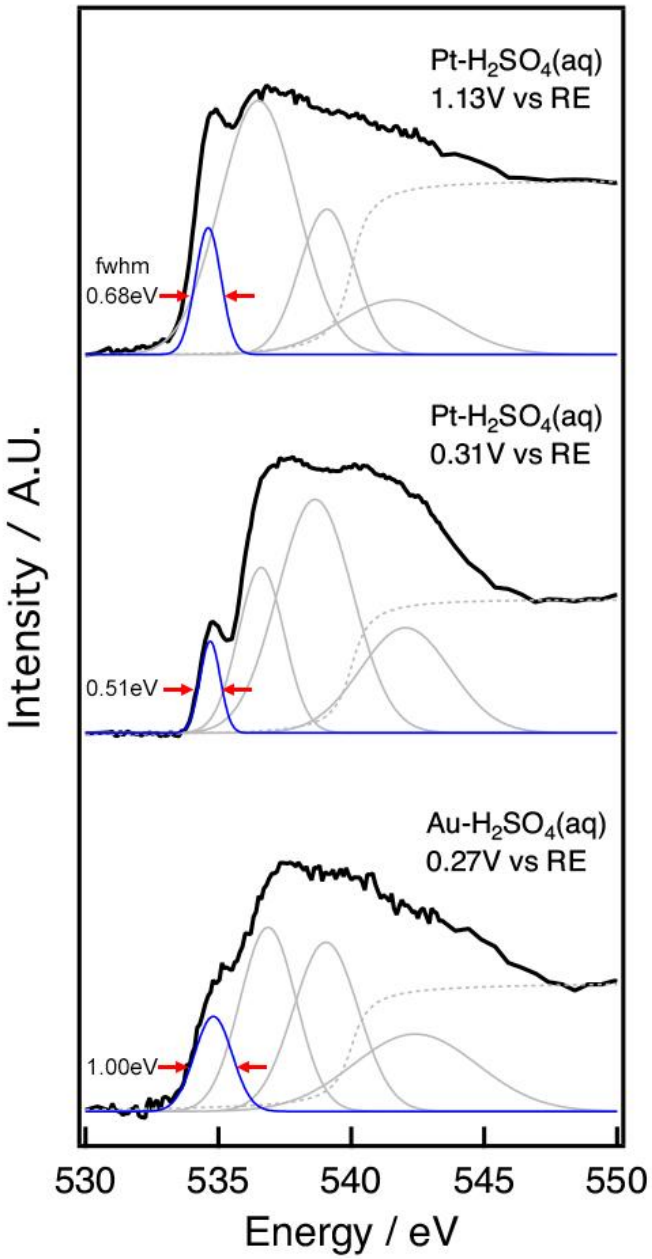

Figure S7. Peak deconvolution of EY-XAS spectra of the Pt-H_2SO_4(aq) interface at 1.13V and 0.31V vs Ag/AgCl (above OCP) and of Au/H_2SO_4(aq) interface at 0.27V vs Ag/AgCl (below OCP).

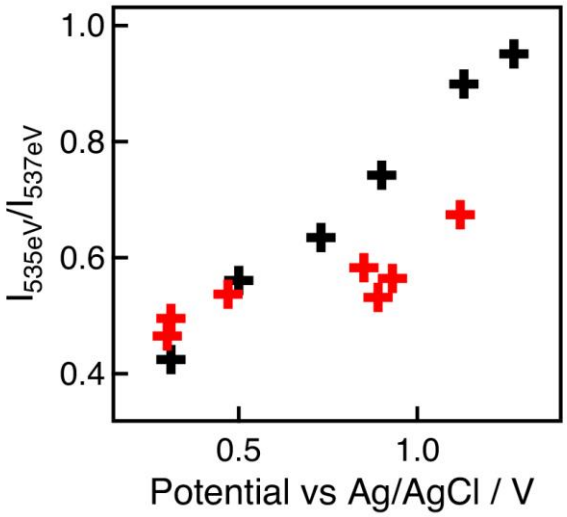

Figure S8. Dependence of pre-peak to main-peak ratios (I_{535eV}/I_{537eV}) in the O K-edge EY-XAS of Pt-H_2SO_4(aq) interface from two sets of experiments. The difference in the slope is possibly due to the change of chemical states of Pt CE during long period experiments at a fixed potential during each spectrum.

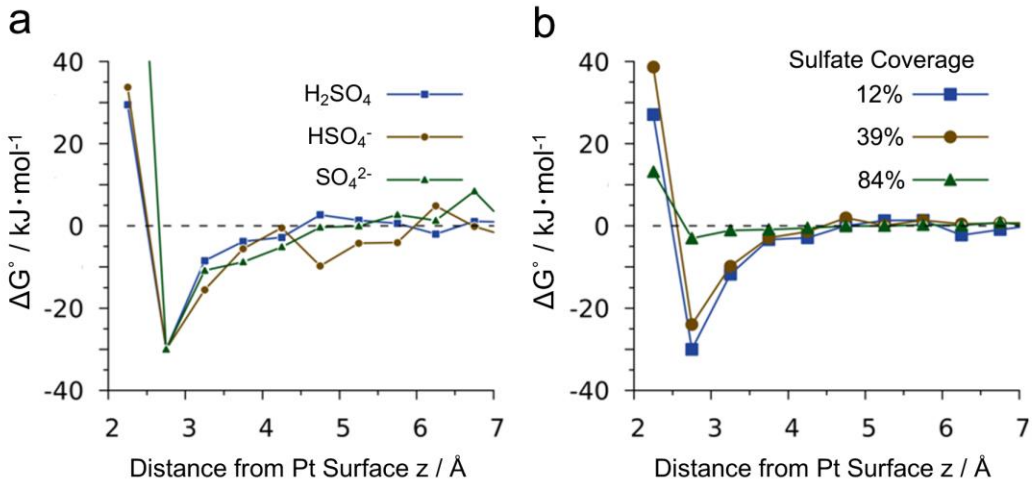

Figure S9. Calculated binding free energy profile of sulfate species at the Pt-H_2SO_4(aq) interface. **(a)** Comparison of profiles of isolated H_2SO_4 (blue squares), HSO_4^- (brown circles) and SO_4^{2-} (green triangles) molecules. **(b)** SO_4^{2-} binding free energy profile at three surface coverages, corresponding to bulk concentration 0.4M, 1.0M, and 3.0M, respectively.

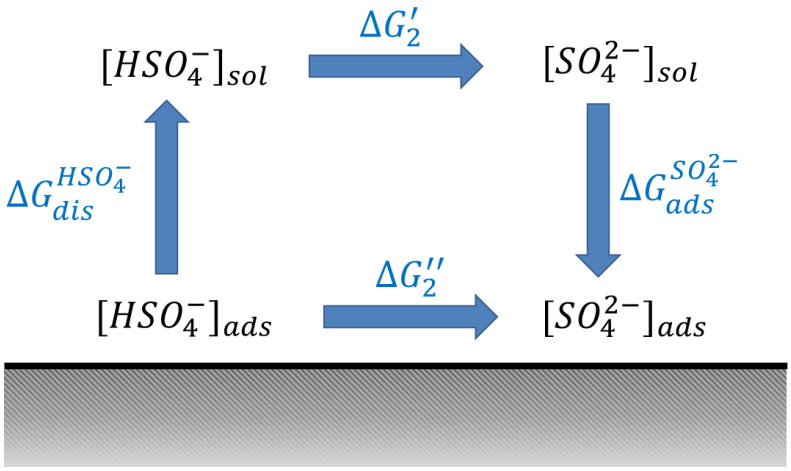

Figure S10. Thermodynamic cycle for evaluation of the equilibrium constant of adsorbed bisulfate ions.

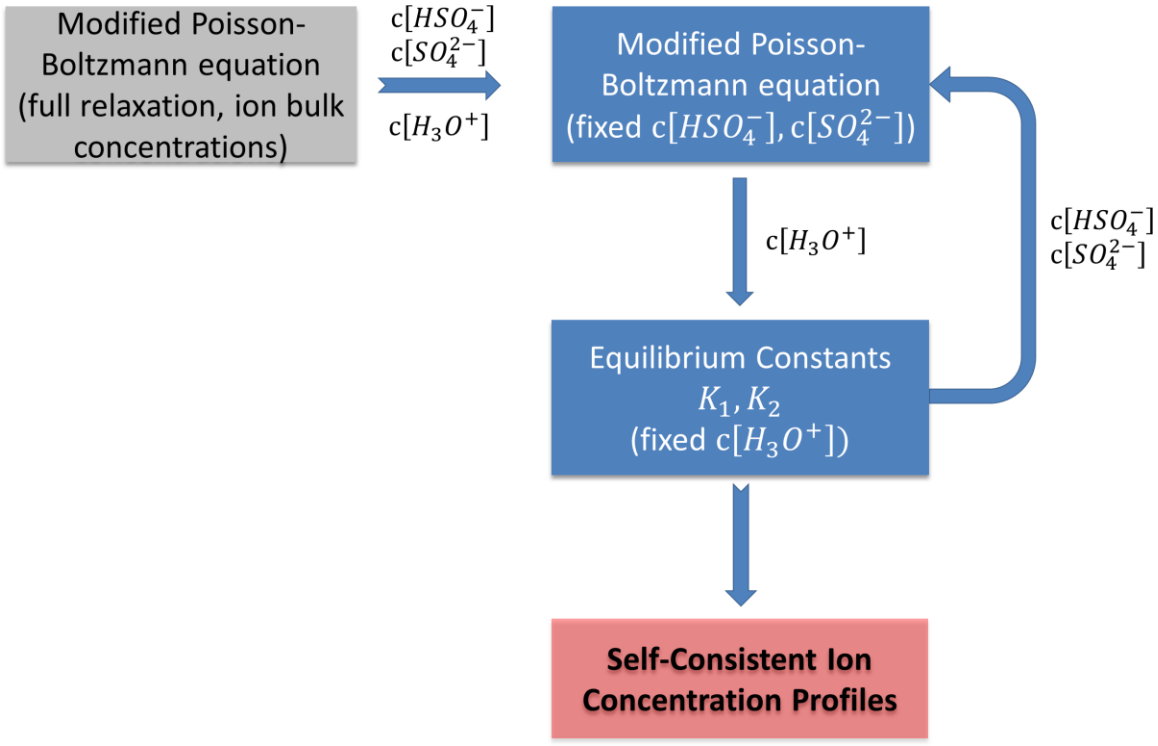

Figure S11. Scheme of the calculation flow towards a self-consistent solution of the modified Poisson-Boltzmann equation with external constraints associated with inter-conversion of sulfate and bisulfate ions.

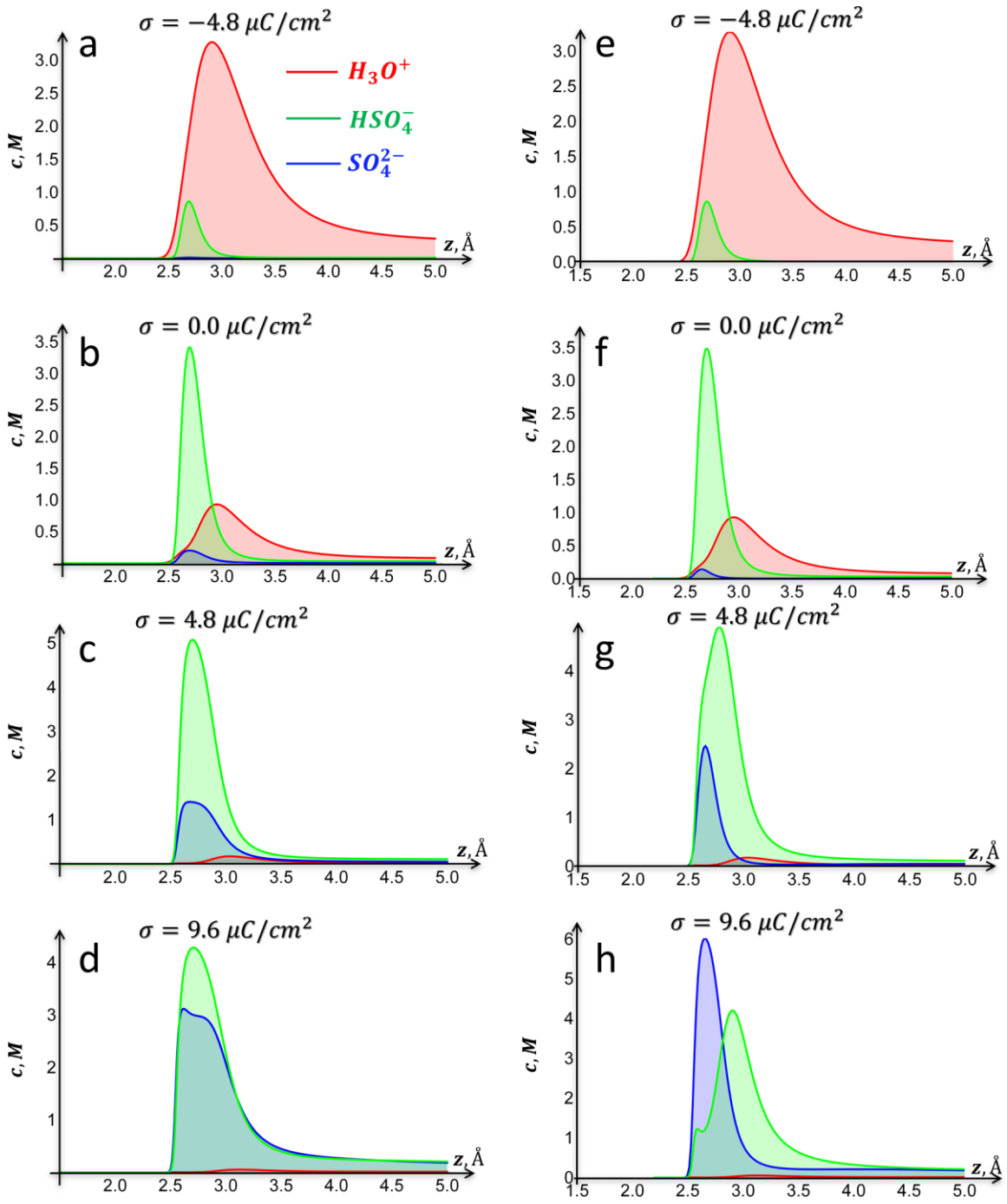

Figure S12. Ion concentration profiles calculated using continuum model without (**a-d**) and with (**e-h**) equilibration of concentrations due to the ion inter-conversion at various surface charge densities.

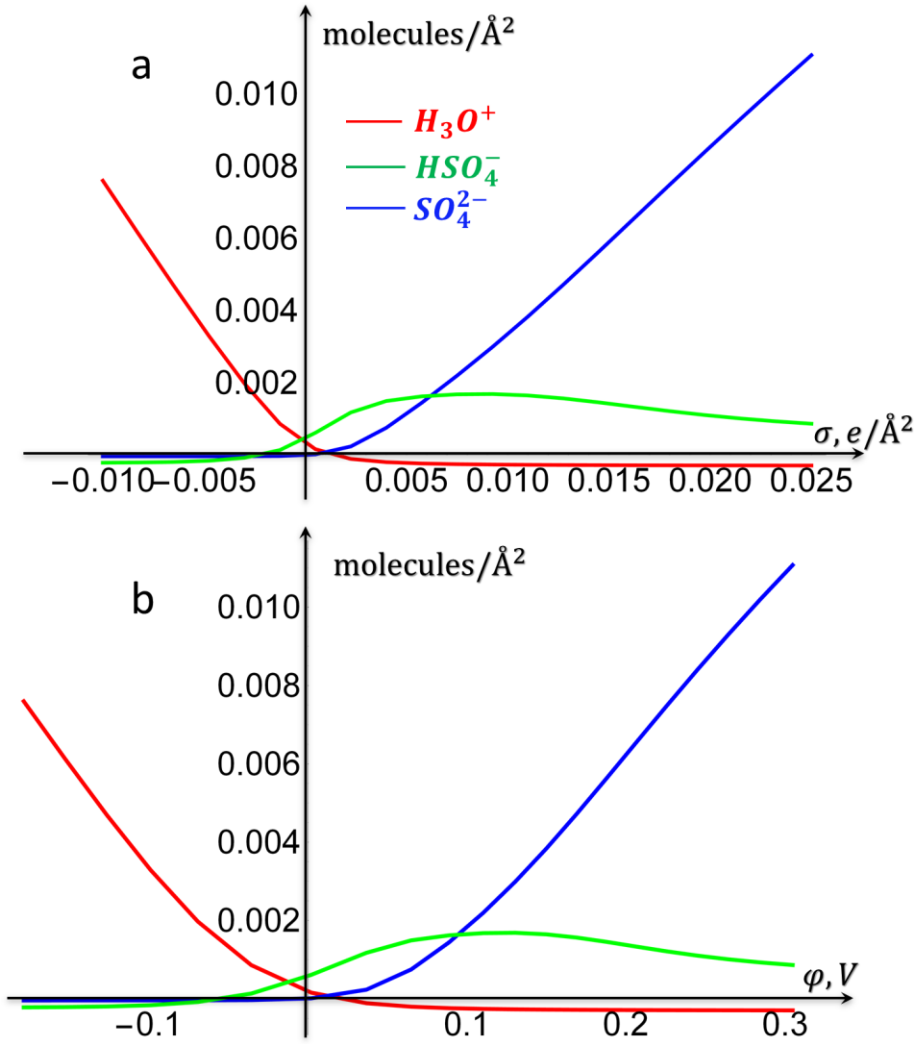

Figure S13. The profiles of surface excess of ions as a function of surface charge density (**a**) and as a function of the electrode potential (**b**). Potentials are referenced to the value in the bulk electrolyte. Negative values on the y axis correspond to deficiency while positive values indicate excess.

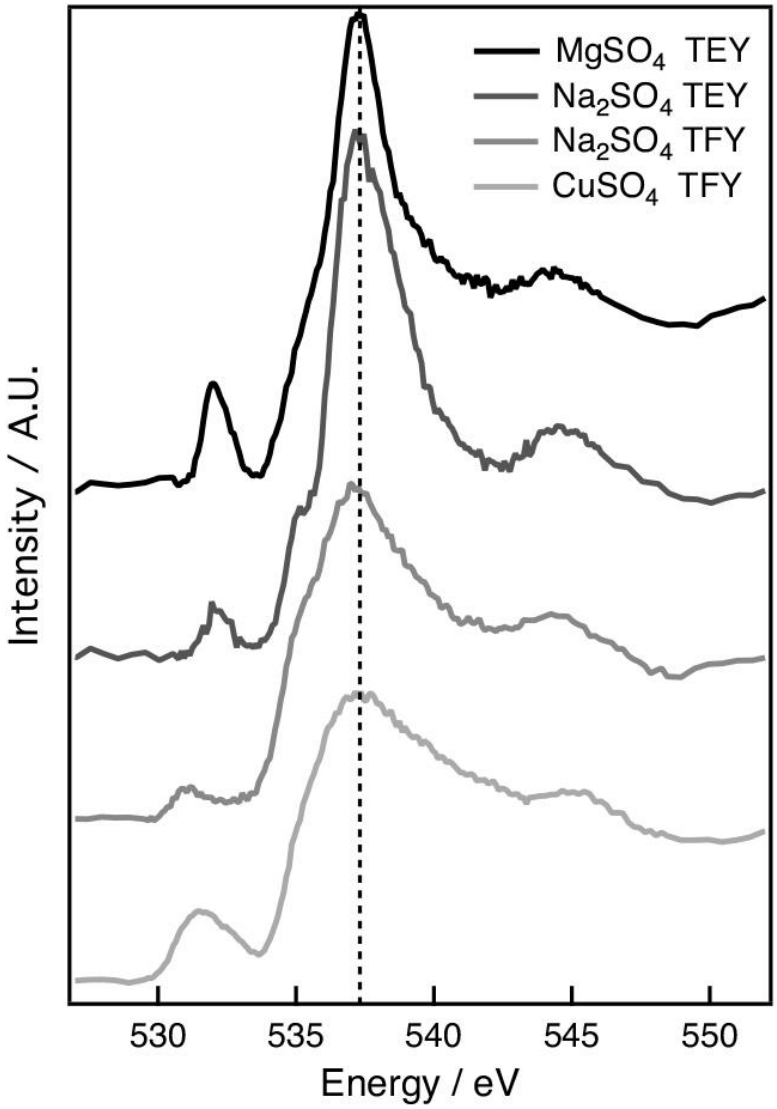

Figure S14. O K-edge XAS spectra of the salt crystals of various sulfates.

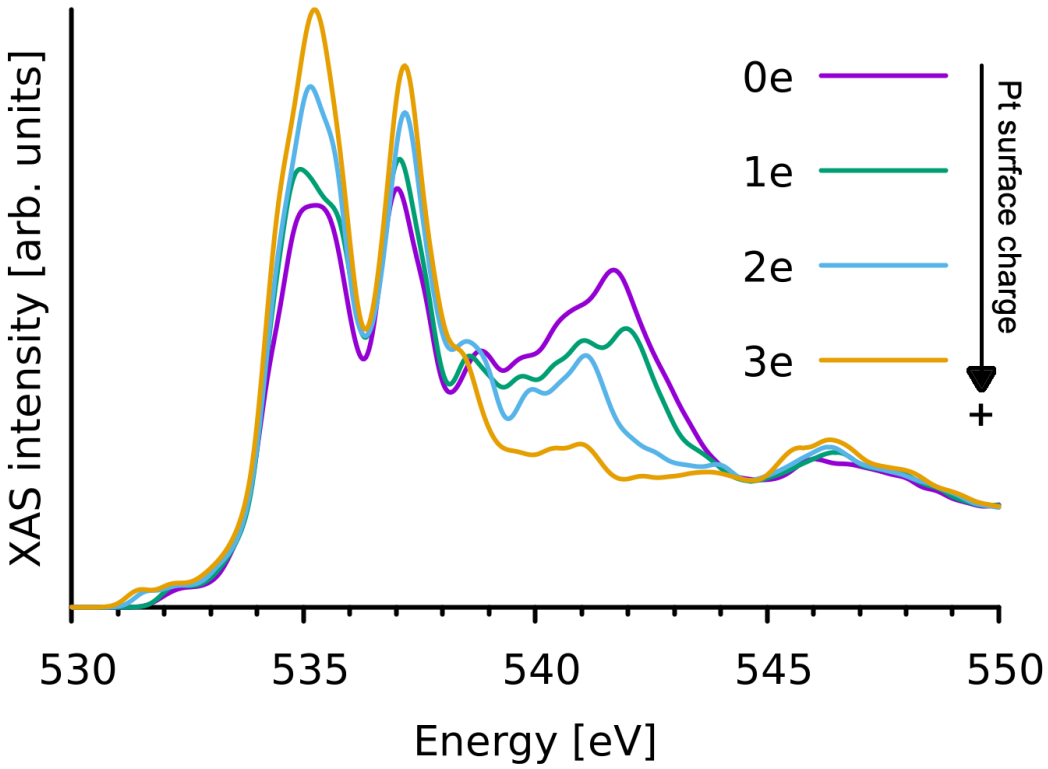

Figure S15. Simulated O K-edge XAS of sulfate (SO_4^{2-}) anions at the Pt-H_2SO_4(aq) interface with different surface charge. Each simulation cell of the size 11.2×9.7×53.4 $Å^3$ containing two sulfate anions and four (purple), three (green), two (blue) and one (brown) hydronium (H_3O^+) cations. Each cell underwent NVT FPMD for 2ps and the resulting spectrum is the numerical average of 20 individual snapshots from the last 1ps FPMD (evenly separated by 50fs).